Post-print of the article:
N. Cancilla, L. Gurreri, G. Marotta, M. Ciofalo, A. Cipollina, A. Tamburini, G. Micale, *A porous media CFD model for the simulation of hemodialysis in hollow fiber membrane modules*, J. Memb. Sci. (2022) 646 120219. https://doi.org/10.1016/j.memsci.2021.120219

# A porous media CFD model for the simulation of hemodialysis in hollow fiber membrane modules

N. Cancilla[a], L. Gurreri[a]*, G. Marotta[b], M. Ciofalo[a], A. Cipollina[a], A. Tamburini[a], G. Micale[a]

[a]*Dipartimento di Ingegneria, Università degli Studi di Palermo (UNIPA), Viale delle Scienze Ed. 6, 90128 Palermo, Italy*

[b]*Medtronic®, via Camurana 1, 41037 Mirandola, Modena, Italy*

*corresponding author: luigi.gurreri@unipa.it

## Abstract

A computational model was developed to predict the performance of hollow fiber membrane hemodialyzers. Blood and dialysate were modelled as fluids flowing through two interpenetrating porous media. Concerning hydrodynamics, experimental Darcy permeabilities measured for commercial hemodialyzers were used for both compartments. Concerning mass transfer, both diffusion and ultrafiltration were simulated. On the blood side theoretical Sherwood numbers for parallel flow in pipes were adopted. On the dialysate side Sherwood numbers were derived from CFD predictions for regular hexagonal fiber bundles. Solute concentrations on the two sides were alternatively computed in an iterative way and were coupled by sink/source terms describing mass transfer. Unlike previous models, the present one is fully predictive, in that it does not use an empirically adjusted global mass transfer coefficient but requires only basic membrane properties (diffusive and hydraulic permeabilities and reflection coefficient). A further novelty is the inclusion of oncotic pressure effects. The model predicts 3-D flow and solute concentration fields and overall performance parameters such as clearance as functions of geometry, flow rates, solute species and membrane properties. In particular, two commercial hemodialyzer configurations were simulated; the predicted clearances of urea and B12 vitamin were found to agree well with experimental measurements.

***Keywords***: *Computational Fluid Dynamics, hemodialysis, hollow fiber membrane, porous media, mass transfer.*

# 1. Introduction

## 1.1 Hemodialysis and hemodialysis modules

In the world, kidney diseases affect today over 850 million people [1]. Two million suffer from End-Stage Renal Disease, and this number increases by 5-7% each year [2]. These figures are expected to rise due to the recent COVID-19 pandemic: according to the US National Institutes of Health, around 5% of the COVID-19 patients are now suffering from acute kidney injury and need renal replacement therapies including hemodialysis [3].

Hemodialysis is a clinical treatment that requires flowing the patient's blood through an external circuit for removing waste solutes before it is pumped back into the body. A typical hemodialysis module, or *hemodialyzer* (**Figure 1**), is a cylindrical shell, ~2-5 cm in diameter and ~15-25 cm in length, enclosing a bundle of several thousands (~8,000-16,000) of hollow fibers (capillary membranes). The shell usually consists of a transparent polymeric material like polycarbonate or polypropylene and bears inlet and outlet openings for the fluids.

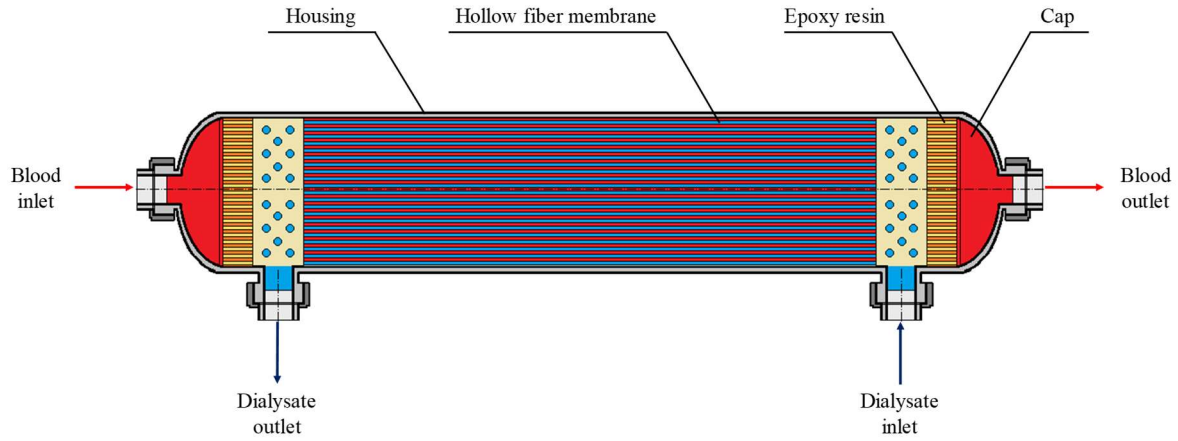


**Figure 1:** Schematic configuration of a typical hollow fiber membrane hemodialyzer.

In these devices two fluids are present: the blood, rich in "toxic substances", and the dialysate, a rinsing solution, separated by the semi-permeable membrane. The dialysate flows outside the bundle of fibers (shell-side) while the blood flows inside the fibers (lumen-side). Since both pressure and solute concentration in blood and dialysate are different, the solutes are removed from blood by *hemodiafiltration*, a combination of ultrafiltration and diffusion [4]. Only if this latter largely prevails, one speaks of *hemodialysis*.

Blood flow rates range from 200 to 500 mL/min (so that the patient's whole blood is typically treated every 15 minutes) and dialysate flow rates from 500 to 800 mL/min.

## 1.2 Hollow fiber module modelling in the literature

Proposed models of hollow fiber membrane-based processes can be classified according to whether the object modelled is a single fiber with the associated lumen-side and shell-side fluids, or the whole hemodialyzer.

Models of the former category, in their turn, can be of increasing complexity in regard to dimensionality (1-D, 2-D, 3-D) and to the physical phenomena described.

In 1-D models [5,6] solute concentrations vary only along the axial direction $z$, as in elementary heat exchanger theory. Phenomena such as the dependence of mass transfer coefficients on the flow conditions, concentration polarization or ultrafiltration flux along the fiber length can be accounted for by simplified correlations [7,8].

Several authors [9–13] presented 2-D ($z$,$r$) models of velocity, pressure and flow concentration for both blood and dialysate.

3-D models are less common in the literature. Cancilla *et al.* [14] performed CFD simulations in ($z$,$r$,$\theta$) coordinates based on the continuity, momentum and scalar transport equations to predict fluid flow and mass transfer in the unit cell of regular bundles of straight parallel fibers arranged in a hexagonal or square lattice. The azimuthal variation of flow and concentration fields was accounted for, but flow and mass transfer were assumed to be fully developed in the axial direction $z$. Eloot *et al.* [15] developed a 3-D finite volume microscale model for fibers arranged in a hexagonal lattice; for symmetry reasons, only a twelfth part of a unit cell was simulated. Non-Newtonian blood behavior was considered.

In a second category of models, the object modelled is the whole module. Conceptually, a "brute force" approach simulating the whole fiber bundle would be possible, but it would imply an inordinate computational effort since, as mentioned above, a typical module may include $10^4$ fibers or more. On the other hand, an oversimplified approach can be adopted, in which the results obtained for a single unit cell (an individual fiber and the associated fluid regions) are assumed to apply to the whole module. Of course, this approach cannot account for the overall module geometry, e.g. for the influence of walls and inlet-outlet headers.

As a compromise between the above methods, some authors chose to simulate a small fiber bundle, somehow representative of the fiber-fiber interactions occurring in a complete module but, of course, computationally much less demanding. For example, Ma *et al.* [16] simulated the impact of fiber distance and position on fiber-fiber interaction within a 3×3 square array bundle. The simulation predicted the effect of fiber distance on the hydrodynamics and filtration performance of a membrane module.

However, the most popular and effective approach to modelling a whole module is the porous media one. In this, either one or both fluids are assumed to flow in anisotropic porous media, governed by Darcy's law. Hydraulic permeabilities and mass transfer coefficients are derived either from numerical simulations for a single fiber or from experimental results.

Thus, Lemanski and Lipscomb [17] carried out a theoretical 2-D analysis of shell-side flow and its influence on mass transfer. They characterized the bundle by using published theoretical and computational results for Darcy permeabilities [18,19] in regular (hexagonal and square) arrays of parallel fibers, but neglected ultrafiltration.

Liao *et al.* [20] overcame this limit, taking into account in their 2-D model both convection and diffusion by means of source terms representing solution and solute trans-membrane fluxes, as calculated by the Kedem-Katchalsky equations. The shell side was treated as a porous medium and properties such as the membrane's hydraulic and diffusive permeability or the bundle's Darcy permeability were derived from experimental results.

Eloot *et al.* [21] used Single Photon Emission Computed Tomography imaging to validate a 3-D CFD model of the fluid dynamics of a hollow fiber hemodialyzer, in which the blood and dialysate compartments were defined as two porous entities with uniform axial and radial permeabilities.

Other 2-D models based on the concept of two interpenetrating porous media are due to Łabęcki *et al.* [22], Lemanski and Lipscomb [23] and Ding *et al.* [24].

Ding *et al.* [25] implemented a 3-D model of a hemodialyzer the better to account for the effects of inlet and outlet headers and for the interaction between blood and dialysate flows. Darcy permeabilities were derived from equations presented in the literature. In regard to mass transport, the authors employed a global mass transfer coefficient deduced from literature experimental results. The comparison with the ideal counter-flow configuration in terms of solute clearance showed that the real efficiency of the module was lower than the ideal one, especially when the dialysate flow rate was low or the blood flow rate was high.

In the present study, starting from the concept of two interpenetrating porous media, a new model of fluid flow and mass transfer in hollow fiber modules for hemodialysis is developed. To the best of the authors' knowledge, this is the first 3-D model that simultaneously includes:

- values of Darcy permeability both in the axial and in the transverse directions derived from purpose conducted experimental measurements;
- the separate effects of the three resistances of blood, membrane and dialysate on mass

transport;

- the possibility of adopting models of increasing complexity.

Once validated, the present model can be used as a tool for evaluating the effects of membrane properties, module design and operating conditions on the dialyzer's performance.

## 2. Experimental characterization of the hemodialyzers

Two PHYLTHER® High Flux modules, commercialized by Medtronic®, were tested. Their nominal geometric characteristics, as provided by the company, are listed in **Table 1**.

**Table 1:** Nominal geometric characteristics of the hollow fiber modules tested.

| Module type | Membrane material | Nominal internal area $A$ ($m^2$) | Effective length $L$ (mm) | Fiber inner diameter $d_i$ (μm) | Membrane thickness $s$ (μm) | Module inner diameter $D_i$ (mm) |
|---|---|---|---|---|---|---|
| PHYLTER® HF 15SD | Polyphenylene | 1.5 | 244 | 200 | 30 | 37 |
| PHYLTER® HF 17SD | Polyphenylene | 1.7 | 244 | 200 | 30 | 40 |

The effective length $L$ is that of the fibers, not including the end tracts encased in epoxy resin ("pottings", **Figure 1**). The nominal internal area is $A=N_0\pi d_i L$, $N_0$ being a nominal number of fibers which, based on the data in **Table 1**, turns out to be 9784 and 11089, respectively for the two modules. Nominal data were carefully checked as detailed in Section 2.3.

The distribution of hollow fibers in a real hemodialyzer may affect the concentration field as well as the module's wet-out, the entrapment of air bubbles and thus the module's performance, so that it has been made the subject of experimental investigations, e.g. by Frank *et al.* [26,27] who used X-ray computed tomography.

In the present work, for each module type, a first destructive investigation was performed by filling the shell side of the module with a slow curing low viscosity epoxy resin (Denepox 40®). After flushing the shell with resin several times to ensure that all air exited the module, 24 hours were allowed for the resin to harden. Then the module was cut into 25 slices about 5 mm in thickness by using a lathe; the slices were finally polished and then analyzed by various techniques. In a second specimen, the outer shell was cut, the fiber bundle was extracted and a small loose sample was taken from it for further SEM investigation.

### 2.1 SEM analysis

Both slices and loose samples of the fiber bundles were examined by Scanning Electron

Microscopy using the standard gold-coating method. **Figure 2(a)** shows a single fiber, with an outer diameter $d_e$ of 258.9 µm, very close to the nominal value of 260 µm. A comparison of different images showed that this quantity is actually scattered between ~240 and 280 µm, with few individual diameters outside this range. **Figure 2(b)** is a detail of a slice. Straight grooves and debris in the fibers' lumen are artefacts due to the cutting and polishing process. The cluster of small dots near the center of the picture is the cross section of a spacing polymeric yarn which is intentionally interspersed with the fiber bundle during the manufacturing process in order to give it structure, avoiding fibers from moving laterally and collapsing. The characteristics of the yarn are better visible in **Figure 2(c)**, which shows a single hollow fiber close to a tuft of spacing yarn, and in **Figure 2(d)**, which is an enhanced detail of the yarn showing filament diameters varying between ~20 and ~27 µm.

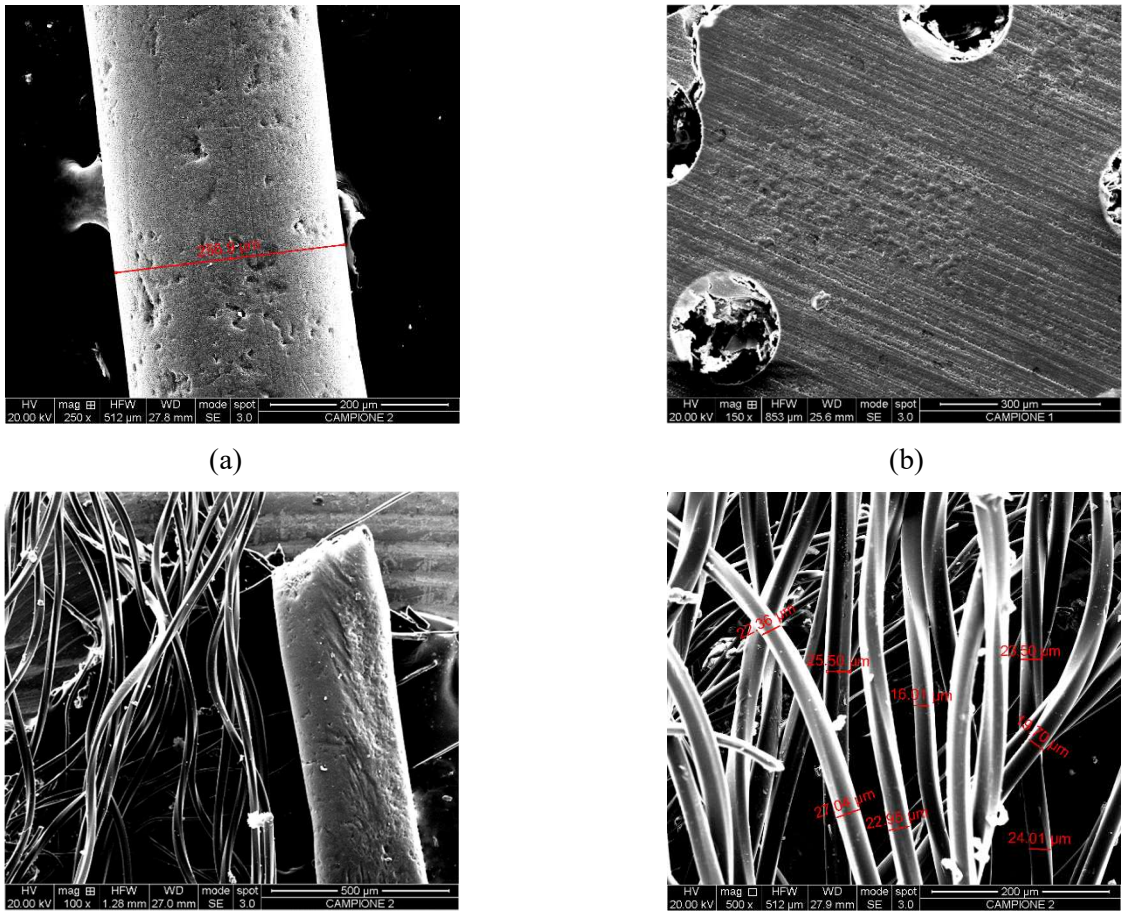


(a) (b)

(c) (d)

**Figure 2:** SEM images of the samples analyzed: (a) individual fiber, showing external diameter; (b) resin-embedded bundle slice with cross section of a tuft of spacing yarn; (c) single fiber surrounded by spacing yarn; (d) spacing yarn detail, showing typical filament diameters.

## 2.2 Optical microscopy

Slices of the resin-embedded bundle were further analyzed by optical microscopy. **Figure 3** shows pictures of a cross-section. It can be observed that, in regions devoid of spacing yarn (a), fibers are more densely packed and tend to arrange themselves into almost regular hexagonal-array clusters. In the presence of spacing yarn tufts (b), fibers are prevented from densely packing and thus form high-porosity, irregularly scattered, regions.

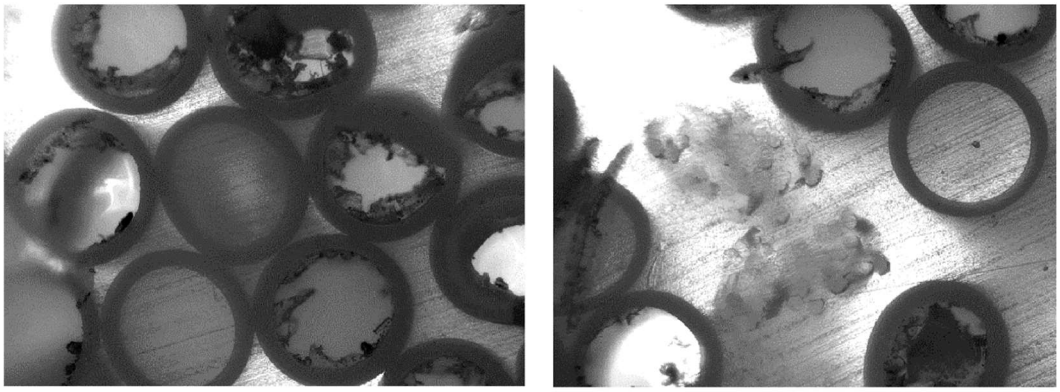

(a) (b)

**Figure 3:** Pictures realized by optical microscopy: (a) region of higher fiber packing density and (b) region of lower packing density where the presence of spacing yarns can be observed.

## 2.3 Fiber number and distribution

Slices were photographed in backlighting using a macro lens, obtaining images like those reported in **Figure 4**(a) and (b), respectively for the two modules. The images, converted to greyscale and improved by enhancing contrast and sharpness using the Corel PaintShop Pro® software, were analyzed both by the MATLAB® function *imfindcircles* and by a purpose written Fortran program to count the actual number of fibers. Both methods agreed to within a few units in counting ~9940 and ~11450 hollow fibers for the two modules, respectively. The discrepancy with respect to the nominal fiber numbers reported above (9784 and 11089, respectively), deduced from nominal internal areas, is small (+1.6-3.3%). For a nominal outer fiber diameter of 260 μm, the actual fiber numbers correspond in both cases to a porosity (shell side area/total cross sectional area) of ~0.51.

The examination of cross-sections like those in **Figure 4** shows that fibers are not randomly distributed in the bundle, but exhibit the presence of *clusters*. Based on the previous discussion, this can be explained by the effects of the spacing yarn, which itself is not visible at the low magnification of **Figure 4**. There is no evidence of the radial porosity gradient observed by Frank *et al.* [26,27], but this can be due to the large difference in packing

density, membrane material and inlet-outlet manifold configuration.

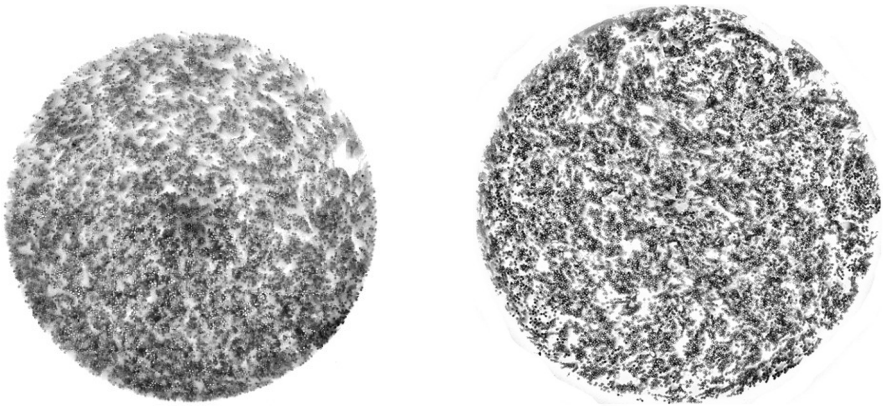

(a) (b)

**Figure 4:** Photographs of two arbitrary slices of modules PHYLTER® HF 15SD (a) and PHYLTER® HF 17SD (b) (drawn to scale).

## 2.4 Hydraulic resistance measurements

The hydraulic resistance $\Delta p/Q$ of the fiber bundles was experimentally determined both in purely longitudinal and in purely transverse flow. Details of the experimental technique and of the results are reported in the **Supplement**, which also contains a discussion of the discrepancies between the experimental conditions and the actual operating conditions of a hemodialyzer. Measured raw hydraulic resistances are summarized in **Table 2**; each value is the average of three tests conducted with different modules / bundles sharing the same nominal membrane area. The results of the three tests differed by a few percent.

**Table 2:** Measured hydraulic resistances $R$ ($Pa \cdot s \cdot m^{-3}$)

| Compartment and flow direction | PHYLTER® HF 15SD | PHYLTER® HF 17SD |
|---|---|---|
| Lumen, axial flow (*af*) | $6.507 \cdot 10^8$ | $5.636 \cdot 10^8$ |
| Shell, axial flow (*af*) | $4.241 \cdot 10^8$ | $4.880 \cdot 10^8$ |
| Shell, cross flow (*cf*) | $5.866 \cdot 10^8$ | |

Measured hydraulic resistances in axial and cross flow ($R_{af}$, $R_{cf}$) are better compared with one another and with computational predictions for regular fiber arrays once converted into Darcy permeability. The Darcy permeability $K_z$ along the longitudinal direction $z$ was defined as:

$$K_z = \frac{\mu \cdot L_{af}}{A_{af}} \cdot \frac{1}{R_{af}} \quad (1)$$

The length $L_{af}$ was assumed to be the distance between the fluid's inlet and outlet (26.1 cm

for lumen side, 23 cm for shell side) while the cross sectional area $A_{af}$ of the whole bundle was $\pi D_i^2/4$=10.75 cm$^2$ for the 1.5 m$^2$ module and 12.57·cm$^2$ for the 1.7 m$^2$ one.

The Darcy permeability $K_t$ along the cross-flow direction $t$ was defined as:

$$K_t = \frac{\mu \cdot L_{cf}}{A_{cf}} \cdot \frac{1}{R_{cf}} \tag{2}$$

In this case, the distance $L_{cf}$ over which the pressure drop occurs is 7.6 cm while the cross sectional area $A_{cf}$ of the whole bundle is 21×1.7 cm$^2$ (**Figure S.5** in the Supplement).

The medium was assumed to be hydraulically isotropic in the cross sectional plane, so that $K_t$ did not depend on the direction of the cross flow. This assumption is appropriate to a random fiber distribution, but is essentially valid also in a regular, e.g. hexagonal, fiber lattice [14]. Results are reported in **Table 3**.

**Table 3:** Experimental Darcy permeabilities $K_z$, $K_t$ (m$^2$).

| Compartment and flow direction | PHYLTER® HF 15SD | PHYLTER® HF 17SD |
|---|---|---|
| Lumen, axial flow ($K_{z,B}$) | $3.3\cdot10^{-10}$ | $3.3\cdot10^{-10}$ |
| Shell, axial flow ($K_{z,D}$) | $4.5\cdot10^{-10}$ | $3.4\cdot10^{-10}$ |
| Shell, cross flow ($K_{t,D}$) | $3.2\cdot10^{-11}$ | |

As will be discussed in Section 3.2 (**Table 6**), on the lumen side the above measured values of $K_{z,B}$ are in good agreement with predictions based on the Hagen-Poiseuille flow theory, being about ~8% lower than these latter. On the contrary, on the shell side measured permeability values are ~2.5 times ($K_{z,D}$) and ~11 times ($K_{t,D}$) lower than those predicted by CFD for the flow around a regular hexagonal array of straight indefinite cylinders.

## 2.5 Clearance measurements

The main performance parameter addressed in hemodialysis is the solute clearance. This parameter describes the impact of the dialysis process on the patient and allows the evolution of the toxin concentration in the patient body with time to be predicted. Clearance can be defined as the blood volume which should be completely purified in the time unit to yield a given solute removal rate; an operative definition is

$$\mathrm{CL} = \frac{Q_{Bi}\, C_{Bi} - Q_{Bo}\, C_{Bo}}{C_{Bi}} \tag{3.a}$$

where $Q_{Bi}$ and $Q_{Bo}$ are the blood flow rates at the hemodialyzer's inlet and outlet, respectively, while $C_{Bi}$ and $C_{Bo}$ are the inlet and outlet solute concentrations in the blood.

Eq. (3.a) can also be re-formulated so as to evidence the contribution of the ultrafiltration flow rate $Q_{UF}$, calculated as the difference $Q_{Bi}$–$Q_{Bo}$:

$$\mathrm{CL} = \left(\frac{C_{Bi}-C_{Bo}}{C_{Bi}}\right) \cdot Q_{Bi} + \left(\frac{C_{Bo}}{C_{Bi}}\right) \cdot Q_{UF} \qquad (3.b)$$

Clearance tests were carried out at Medtronic® following a protocol developed according to applicable parts of ISO 8637-1:2017 and Guidance for Premarket Notification §VII.B. Modules were taken randomly from standard production and tests were repeated on several samples for each model. Each test case was performed simulating a treatment and measuring the clearances obtained from 0.9% w/w NaCl solutions representing blood and containing different markers (urea and B12 vitamin) with the concentrations in **Table 4**.

**Table 4:** Molar concentration ranges of the solutes used in the saline water test solution.

| Solute | Molar concentration range |
|---|---|
| Urea (mmol/L) | 15 to 30 |
| B12 vitamin (µmol/L) | 15 to 40 |

The experimental setup is shown in **Figure 5**.

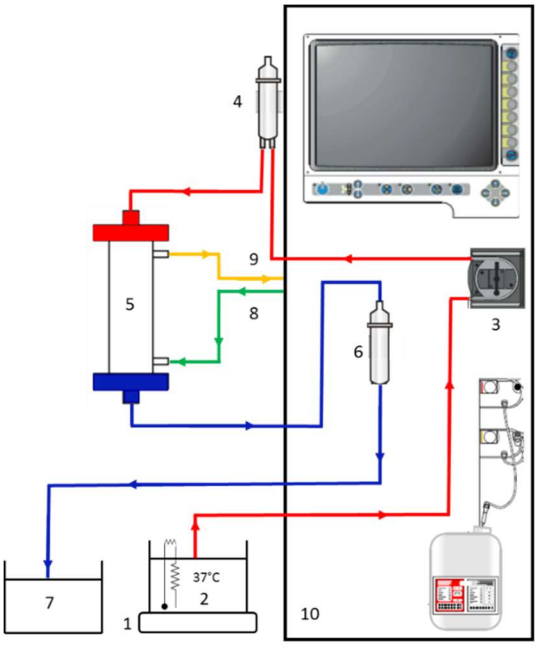


**Figure 5:** Schematic representation of the experimental set up used to measure clearance. (1) magnetic stirrer; (2) beaker for solution storage at 37±1°C; (3) blood pump; (4) and (6) chambers; (5) device under test; (7) beaker for fluid collection; (8) fresh dialysate solution incoming in the dialysate fluid compartment; (9) ultra-filtrate fluid leaving the dialysis fluid compartment; (10) dialysis machine.

All tests were conducted at 37± 1°C. Urea concentrations were measured by a Siemens Dimension EXL 200™ clinical chemistry analyzer. Vitamin B12 concentrations were measured by a spectrophotometer at a wavelength of 550 nm (accuracy=±0.5 nm). Results were obtained for "blood" flow rates $Q_B$ of 200, 300 and 400 mL/min, a dialysate flow rate $Q_D$ of 500 mL/min and an ultrafiltration flow rate $Q_{UF}$ of 10 mL/min. The clearance CL for each solute was calculated using Eq. (3.a).

Clearance results for the two module configurations considered in the present study and for different lumen-side ("blood") flow rates are reported in **Table 5**. Data for urea (MW 60 Da) and B12 vitamin (MW 1355 Da) are representative of low-MW and medium-MW solutes. Each figure is the average of 29 test cases. The results' dispersion is indicated as $\sigma_{CL}$.

**Table 5:** Clearance results for urea and B12 vitamin in the two modules considered (the standard deviation $\sigma_{CL}$ is also reported).

| Module type | Solute | UREA | | | B12 VITAMIN | | |
|---|---|---|---|---|---|---|---|
| | $Q_B$ (mL/min) | 200 | 300 | 400 | 200 | 300 | 400 |
| PHYLTER® HF 15SD | **CL** (mL/min) | 187 | 241 | 289 | 136 | 164 | 181 |
| | $\sigma_{CL}$ (mL/min) | 6.89 | 10.3 | 13.8 | 5.15 | 7.72 | 10.3 |
| PHYLTER® HF 17SD | **CL** (mL/min) | 191 | 249 | 294 | 147 | 164 | 186 |
| | $\sigma_{CL}$ (mL/min) | 6.96 | 10.4 | 13.9 | 7.99 | 12.0 | 16.0 |

# 3. Computational model of the hemodialyzer

## 3.1 Multi-scale approach

Conceptually, the model developed in the present study is based on two-scale approach. In a first stage, small-scale CFD simulations based on the primitive continuity, momentum and scalar transport equations were performed to predict fluid flow and mass transfer around a single straight, axially indefinite, fiber, assumed to be part of a regular bundle. In a second stage, small-scale results were converted into corresponding properties of an equivalent porous medium and simulations at module-scale were conducted for the prediction of the 3-D flow fields and solute concentrations both in the blood and in the dialysate.

However, this scaling-up was actually performed only in regard to mass transfer, where, in the absence of detailed measurements in real yarn-filled bundles, the shell-side Sherwood numbers computed by small-scale CFD predictions for regular fiber arrays were adopted. In regard to the dialysate-side hydraulic permeabilities, as better discussed in the following Section 3.2, unit-cell CFD simulations severely underpredicted the experimental results discussed in Section 2.4, mainly because they did not account for the influence of the spacing

yarn; therefore, the experimental results were used.

### 3.2 Small-scale CFD analysis

Numerical simulations of fully developed, steady-state flow with mass transfer around regular square and hexagonal lattices of fiber bundles were reported by the present authors in previous work [14]. The study was conducted at unit cell-scale, i.e. the computational domain was a repetitive periodic unit of the bundle including a single fiber, with periodic boundary conditions imposed to all variables between opposite boundaries.

In regard to fluid flow, predicted hydraulic permeabilities are reported in **Table 6**.

**Table 6:** Predicted Darcy permeabilities $K_z$, $K_t$ for a regular hexagonal lattice.

| Compartment and flow direction | Porosity $\varepsilon$ (-) | Permeability ($m^2$) |
|---|---|---|
| Lumen, axial flow ($K_{z,B}$) | 0.29 | $3.58 \cdot 10^{-10}$ |
| Shell, axial flow ($K_{z,D}$) | 0.51 | $8.64 \cdot 10^{-10}$ |
| Shell, cross flow ($K_{t,D}$) | 0.51 | $3.69 \cdot 10^{-10}$ |

For the lumen side flow, the axial Darcy permeability calculated by the Hagen-Poiseuille theory (yielding a friction coefficient of 64/Re) for the current porosity $\varepsilon_B$=0.29 is $K_{z,B}$=3.58×10$^{-10}$ m$^2$. This result agrees fairly well with the experimental data in **Table 3**, overpredicting them by only ~8%; such discrepancy can be sufficiently explained by the irregular shape and diameter of actual hollow fibers and by their slightly winding axis. The transverse permeability $K_{t,B}$ can be set to zero.

For the shell-side flow, for a hexagonal lattice of cylindrical fibers with porosity $\varepsilon_D$=0.51, equal to that of the tested modules, CFD predicted axial and transverse shell side permeabilities $K_{z,D}$=8.64×10$^{-10}$ m$^2$ and $K_{t,D}$=3.69×10$^{-10}$ m$^2$. As anticipated in Section 2.4, these computational values are ~2.5 times (axial) and ~11 times (transverse) higher than the experimental ones in **Table 3**. Most of this large discrepancy can probably be attributed to the influence of the spacer yarn interspersed with the fiber bundle, with a possible minor influence of the irregular fiber distribution (clustering) and of the winding axis of the hollow fibers. Whatever its reason, this discrepancy makes the adoption of hydraulic permeability values provided by the small-scale simulations [14] in the porous-media model inappropriate and explains the need for experimental measurements.

In regard to mass transfer, the shell-side Sherwood number was defined as:

$$\mathrm{Sh}_D = \frac{\bar{J} \cdot d_h}{D_D \cdot (\bar{C}_{wall} - C_{bulk})} \tag{4}$$

where $\bar{J}$ is the surface-averaged mass flux; $d_h$ is the hydraulic diameter $4V_f/A_{ext}$ (with $V_f$ the volume of dialysate and $A_{ext}$ the outer fiber surface); $D_D$ is the solute's diffusivity in the dialysate; and $\bar{C}_{wall}$, $C_{bulk}$ are the solute's surface-averaged wall concentration and bulk (mass flow averaged) concentration, respectively.

A suitable correlation of the CFD results for regular hexagonal lattices having a porosity of 0.51, equal to that of the modules investigated, is:

$$\mathrm{Sh}_D = a\,(1 + b \cdot \mathrm{Re}_t^{\,c}) \tag{5}$$

where $\mathrm{Re}_t$ is the cross-flow Reynolds number $u_t d_h \rho/\mu$, $u_t$ being the superficial velocity component in the plane of the bundle's cross section. For $a$=9.85, $b$=1.41 and $c$=0.38, Eq. (5) fits well the CFD results in the range $\mathrm{Re}_t$=0.005-50 as shown in **Figure 6**.

The coefficient $a$ is chosen so that, for $\mathrm{Re}_t$=0, the correlation provides the value computed for purely axial flow. The Sherwood number predicted by Eq. (5) is an average over all possible directions of the transverse flow with respect to a regular lattice, as seems appropriate for an irregular fiber distribution. The results in [14] showed that the transverse flow orientation has negligible effects on the Sherwood number at the low values of $\mathrm{Re}_t$ (~0.1-1) expected in a real hemodialyzer.

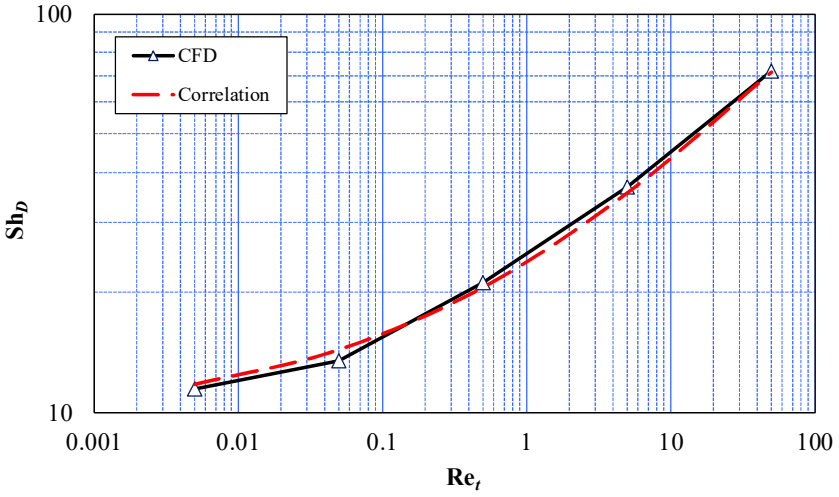


**Figure 6:** Shell-side Sherwood number ($\mathrm{Sh}_D$) in mixed flow as a function of the cross-flow Reynolds number $\mathrm{Re}_t$. The figure shows CFD results along with Eq. (5) written for $a$=9.85, $b$=1.41 and $c$=0.38.

For the lumen side Sherwood number a constant value of 4 can be used, intermediate between the exact values for uniform wall concentration and uniform wall mass flux (3.66 and 4.36,

respectively) [28].

The above defined Sherwood numbers strictly apply only to non-transpiring walls and, in principle, should be modified to account for the influence of ultrafiltration (wall transpiration). However, a recent paper on this issue [29] indicates that, for the present values of trans-membrane solution and solute mass fluxes, this influence is negligible.

In regard to the influence of entry effects on the Sherwood number, for parallel flow the Graetz theory predicts a mass-transfer development length $z^{DEV} \approx 0.02 d_h \mathrm{ReSc}$ [28]. For the nominal hemodialyzer configurations considered here, on both lumen and shell sides one has Re≈5, Sc≈500 (urea) and $d_h \approx 2 \cdot 10^{-4}$ m, so that $z^{DEV} \approx 0.01$ m. Therefore, entry effects are limited to a few percent of the module's length. Moreover, on the shell side this length is less than the extent of the inlet (and outlet) region in which the flow is largely radial and the whole Graetz theory does not apply: in this region the influence of flow three-dimensionality (explicitly accounted for in the CFD model) is dominant on Graetz-type entry effects.

### 3.3 Porous media approach

As anticipated in Section 3.1, in the present study the fluid on either side (blood or dialysate) was assumed to flow in its own equivalent porous medium.

Each porous medium was described by specifying a porosity $\varepsilon$ and adding the following momentum source terms to the right hand side of the momentum (Navier-Stokes) equations, written in Cartesian coordinates $x$, $y$, $z$ ($z$ being parallel to the module's axis and $x$, $y$ lying in the cross sectional plane):

$$S_{M,x} = -\frac{\mu}{K_t} \langle u_x \rangle \tag{6}$$

$$S_{M,y} = -\frac{\mu}{K_t} \langle u_y \rangle \tag{7}$$

$$S_{M,z} = -\frac{\mu}{K_z} \langle u_z \rangle \tag{8}$$

where $\langle u_x \rangle$, $\langle u_y \rangle$ and $\langle u_z \rangle$ are the superficial velocities along the $x$, $y$ and $z$ directions, respectively. For the permeabilities $K_z$ and $K_t$, the experimental values summarized in **Table 3** (Section 2.4) were adopted in most simulations. For comparative purposes only, some cases were run by using the CFD-derived values reported in **Table 6** (Section 3.2), though largely contradicted by the experiments.

As already mentioned, the porosity $\varepsilon$ was set to 0.51 on the shell side and to 0.29 on the lumen side.

In order to account for ultrafiltration (UF), the following mass source term (kg $m^{-3}$ $s^{-1}$) was

added to the right hand side of the continuity equation:

$$S_M = \pm \frac{A_{ext}}{V_{tot}} \cdot \rho \cdot L_p \cdot (p_B - p_D - p_{onc}) \tag{9.a}$$

in which the "plus" sign holds for dialysate and the "minus" sign for blood. Here, $A_{ext}$ is the total external area of the hollow fibers, $V_{tot}$ is the total volume of the module, $L_p$ is the membrane's hydraulic permeability and $p_{onc}$ is the oncotic pressure of proteins in the blood. Similarly, in order to account for UF solute mass flux, the following source term (in mol $m^{-3}$ $s^{-1}$) was added to the right hand side of the solute's scalar transport equation:

$$S_c = \pm \frac{A_{ext}}{V_{tot}} \cdot \left[ L_p \cdot (p_B - p_D - p_{onc}) \cdot (1 - \sigma) \cdot C_{s,M} + U \cdot (C_B - C_D) \right] \tag{9.b}$$

where $\sigma$ is Staverman's reflection coefficient and $C_{s,M}$ is the solute concentration in the fluid crossing the membrane. In different studies, $C_{s,M}$ has been variously expressed as the arithmetic mean $(C_B+C_D)/2$ [20] or the logarithmic mean $(C_B-C_D)/\ln(C_B/C_D)$ [25] of the lumen-side and shell-side bulk concentrations $C_B$, $C_D$. A further alternative would be to identify $C_{s,M}$ with the upstream bulk concentration, i.e. with $C_B$ if the ultrafiltration flux is from blood to dialysate and $C_D$ otherwise. All the above methods were tested in the preliminary development of the present model and no significant difference in the results was observed. For simplicity, the first of the described alternatives was adopted in all final runs, i.e. $C_{s,M}$ was computed as the arithmetic mean of $C_B$ and $C_D$.

The second term in square brackets of Eq. (9.b) represents diffusive mass transport, for which the driving force is the difference in concentration. $U$ is an overall mass transfer coefficient, which can be expressed as:

$$U = \frac{1}{\frac{1}{k_B} + \frac{1}{k_M} + \frac{1}{k_D}} \tag{10}$$

where $k_B$, $k_M$ and $k_D$ are the mass transport coefficients relative to blood, membrane and dialysate. Strictly, Eq. (10) applies to a planar membrane geometry, but it is almost universally adopted in the literature also for the cylindrical geometry of hollow fibers; the coefficients $k_B$ and $k_M$ can be assumed to absorb the relevant geometrical corrections.

The blood side mass transfer coefficients $k_B$ can be calculated as:

$$k_B = \mathrm{Sh}_B \frac{D_B}{d_i} \tag{11}$$

in which $D_B$ is the solute diffusivity in the blood, $d_i$ is the internal diameter of the hollow fibers and $\mathrm{Sh}_B$ is the intra-lumen (blood side) Sherwood number. As anticipated in Section

3.2, a value of 4 was used for this quantity. In the model development stage, it was found that letting $Sh_B$ vary between 3.66 and 4.36 did not affect the results to any significant extent.

The dialysate side mass transfer coefficient $k_D$ was expressed as:

$$k_D = \mathrm{Sh}_D \frac{D_D}{d_h} \tag{12}$$

in which $d_h$ is the hydraulic diameter of the fiber bundle, $D_D$ is the solute diffusivity in the dialysate and $Sh_D$ is the shell-side Sherwood number for which Eq. (5) was used, thus expressing it as a function of the shell-side cross-flow Reynolds number $Re_t$ and as an average over all possible cross flow directions. For comparison purposes only, some simulations were run assuming $Sh_D$ to be equal to that for purely axial flow around parallel and regular fiber bundles at $\varepsilon$=0.51 (9.85); comparative results will be discussed in Section 4.2.2.

The term $k_M$ in Eq. (10) represents the membrane's diffusive permeability for the given solute. It depends on the membrane structure and composition and on its thickness, which usually ranges from ~10 to ~50 μm. The current trend is towards increasing values of $k_M$, which, of course, increase the achievable clearance for given membrane area and solutions concentration. Throughout this work, we used the values of $k_M$ for polyphenylene membranes relative to the two solutes considered (urea and B12 vitamin), which are reported, together with the hydraulic permeability, in **Table 7**. These data, provided by Medtronic®, are not very distant from experimental measurements conducted by Liao *et al.* [30] for similar membranes.

**Table 7:** Membrane properties used in the present simulations.

| Membrane property | Urea | B12 vitamin |
|---|---|---|
| $k_M$ (m s$^{-1}$) | $(1.1 \pm 0.2) \times 10^{-5}$ | $(3.1 \pm 0.2) \times 10^{-6}$ |
| $L_p$ (m s$^{-1}$ Pa$^{-1}$) | $(6.6 \pm 0.4) \times 10^{-11}$ | |

In Eq. (10) the three components (blood, dialysate and membrane) are viewed as resistances in series. The identification of the "controlling" step, that contributes most to the overall resistance to mass transfer, can play a key role in the study of solute removal. With reference to two important solutes, i.e. urea and B12 vitamin, such estimate was conducted assuming:

- fiber bundle geometry as in **Table 1;**
- membrane diffusive permeabilities as in **Table 7**;
- solute diffusivities in blood and dialysate as in **Table 8**, where the relevant literature

sources are also reported;

- Sherwood numbers of 4 for the blood side and 9.85 for the dialysate side (corresponding to purely axial flow), as discussed in Section 3.2.

**Table 8:** Fluids and solutes properties at 37°C.

| Fluid | Density (approx, kg $m^{-3}$) | Viscosity (Pa s) | Diffusivity ($m^2$ $s^{-1}$) | Schmidt number | Inlet concentration (mol $m^{-3}$) | Inlet volume flow rate (mL $min^{-1}$) |
|---|---|---|---|---|---|---|
| Blood | 1000 | $3.5\times10^{-3}$ [31] | $7.4\times10^{-10}$ (urea) [31]<br>$4.0\times10^{-10}$ (B12) [31] | 4730<br>8750 | 20 (urea)<br>$3\times10^{-2}$ (B12) | 300 |
| Dialysate | 1000 | $7.62\times10^{-4}$ [32] | $1.8\times10^{-9}$ (urea) [33]<br>$5.0\times10^{-10}$ (B12) [34] | 500<br>2140 | 0 | 500 |

Results are summarized in **Figure 7**. It shows that, for current high-flux modules, more than half of the resistance to mass transport is located in the membrane, in agreement with the literature [35,36]. This is particularly true for solutes with large molecular weight such as B12 vitamin (1355 Da [32]), while for smaller solutes such as urea (60 Da [32]), the resistance of the blood compartment plays a larger role.

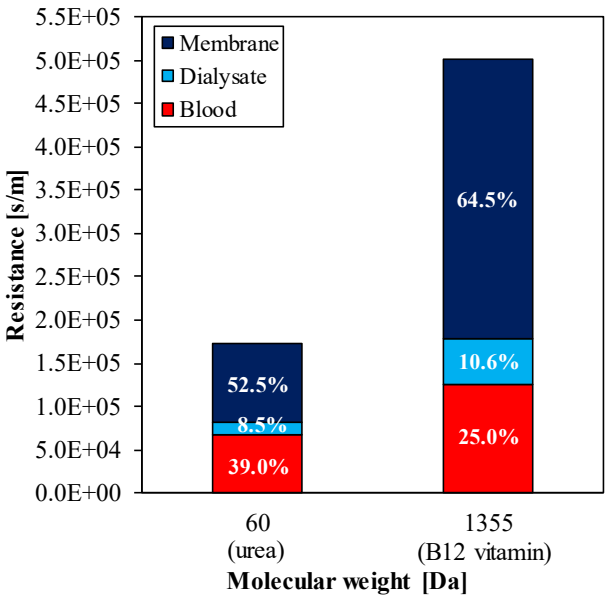


**Figure 7:** Contributions to the overall mass transfer resistance (in s/m) for two solutes.

### 3.4 Computational domain

**Figure 8** shows the computational domain for the modules simulated. Arrows indicate the flow direction for blood (red) and dialysate (black). The computational domain exhibits eight inlets and eight outlets for the dialysate flow, which simulate the presence of a fluid

distributor. Two geometries, representative of the PHYLTHER ® HF 15SD and 17SD modules and differing only for the module's inner diameter (3.7 and 4 cm, respectively) were simulated.

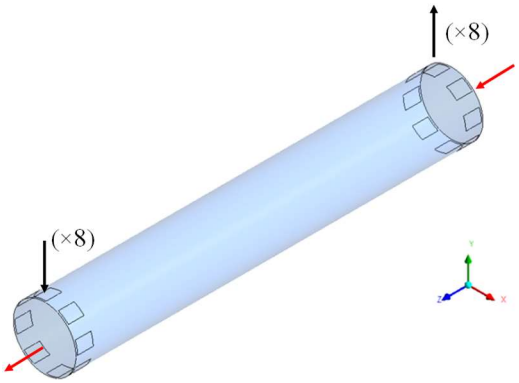


**Figure 8:** 3-D computational domain for the simulated modules.

### 3.5 Simulation strategy

The computational model was developed by means of the finite volume code Ansys-CFX 18® [37], already applied by the authors to the simulation of different low-Reynolds number flow and mass transfer problems in complex geometries, e.g. [38]. As mentioned in Section 3.3, blood and dialysate were treated as two different fluids flowing through two different porous media, but occupying the same space (the whole internal volume of the module) and exchanging both solution and solute between each other. This made an iterative simulation method necessary: flow rates and solute concentrations on the blood and dialysate sides were coupled by appropriate sink/source terms describing solute transfer and were alternatively re-computed until convergence was attained.

**Figure 9** is a flow chart of the computational process. Each fluid, denoted by subscript "*B*" for blood and subscript "*D*" for dialysate, was characterized by its physical properties $\rho$, $\mu$, $D$, inlet volume flow rate $Q$ and inlet concentration $C_i$ (**Table 8**) and by its relevant inlets and outlets configuration. It was assumed to flow through a porous medium with porosity $\varepsilon$, longitudinal permeability $K_z$ and transverse permeability $K_t$ (azimuthally isotropic in the cross-section plane $xy$). Values of these quantities were taken from the experimental characterization and the hydraulic resistance measurements described in Sections 2.3-2.4 and in the **Supplement**. The shell-side Sherwood number was expressed by Eq. (5).

In the simulations reported in the present work, the solute markers were assumed to be urea and B12 vitamin (MW = 60 and 1355 Da, respectively), for which Staverman's reflection coefficients $\sigma$ equal to zero and 0.15, respectively, were used. The hydraulic permeability $L_p$

494 of the membrane and its diffusive permeabilities $k_M$ for the above solutes were those in **Table**
495 **7**.
496 The internal cylindrical surface of the shell was treated as a no slip wall with zero mass flux.
497 In most cases, the outlet boundary conditions for both blood and dialysate were of imposed
498 pressure, while the inlet boundary conditions were of imposed flow rate. The dialysate outlet
499 pressure was set to zero (relative) while the blood outlet pressure was adjusted so as to obtain
500 an ultrafiltration flow rate of 10 mL/min as in corresponding experimental clearance tests. In
501 some comparative cases, representing experimental tests as discussed in the **Supplement**,
502 these conditions were replaced by imposed zero flow rate at both inlets and outlets. The same
503 computational grid was adopted for the two fluids.
504 The computational procedure starts with the first iteration on the blood side (iteration
505 BLOOD 1). In this step, in the mass transfer source term $S_c$ of Eq. (9.b) (written for blood,
506 i.e. with the minus sign) the dialysate-side pressure $p_D$ and concentration $C_D$ are assumed to
507 be zero. At the end of this iteration step, the computed blood-side pressure $p_B$ and
508 concentration $C_B$ fields are written to the special Blood-Side Data File "BSDF[1]".
509 The subsequent simulation (iteration DIAL 1) regards the dialysate side. Here, in the mass
510 transfer source term $S_c$ of Eq. (9.b) (written for the dialysate, i.e. with the plus sign), the
511 pressure $p_B$ and blood-side concentration $C_B$ are read in from the above mentioned special
512 data file. At the end of this iteration step, the computed dialysate-side pressure $p_D$ and
513 concentration $C_D$ fields are written to the special Dialysate-Side Data File "DSDF[1]".
514 In all the subsequent couples of iterations (BLOOD N – DIAL N), each side reads in the last
515 available concentration and pressure distributions for the opposite side from the relevant
516 special data file and write its own computed pressure and concentration to a similar special
517 data file.
518 Convergence is considered fully achieved and the iterative procedure is stopped when the
519 differences in outlet flow rate and solute concentration between two consecutive iterations,
520 both for blood and dialysate, become lower than a fixed tolerance (*TOL*). In all cases,
521 convergence to within 0.5% was achieved in 6-9 couples of iterations.
522

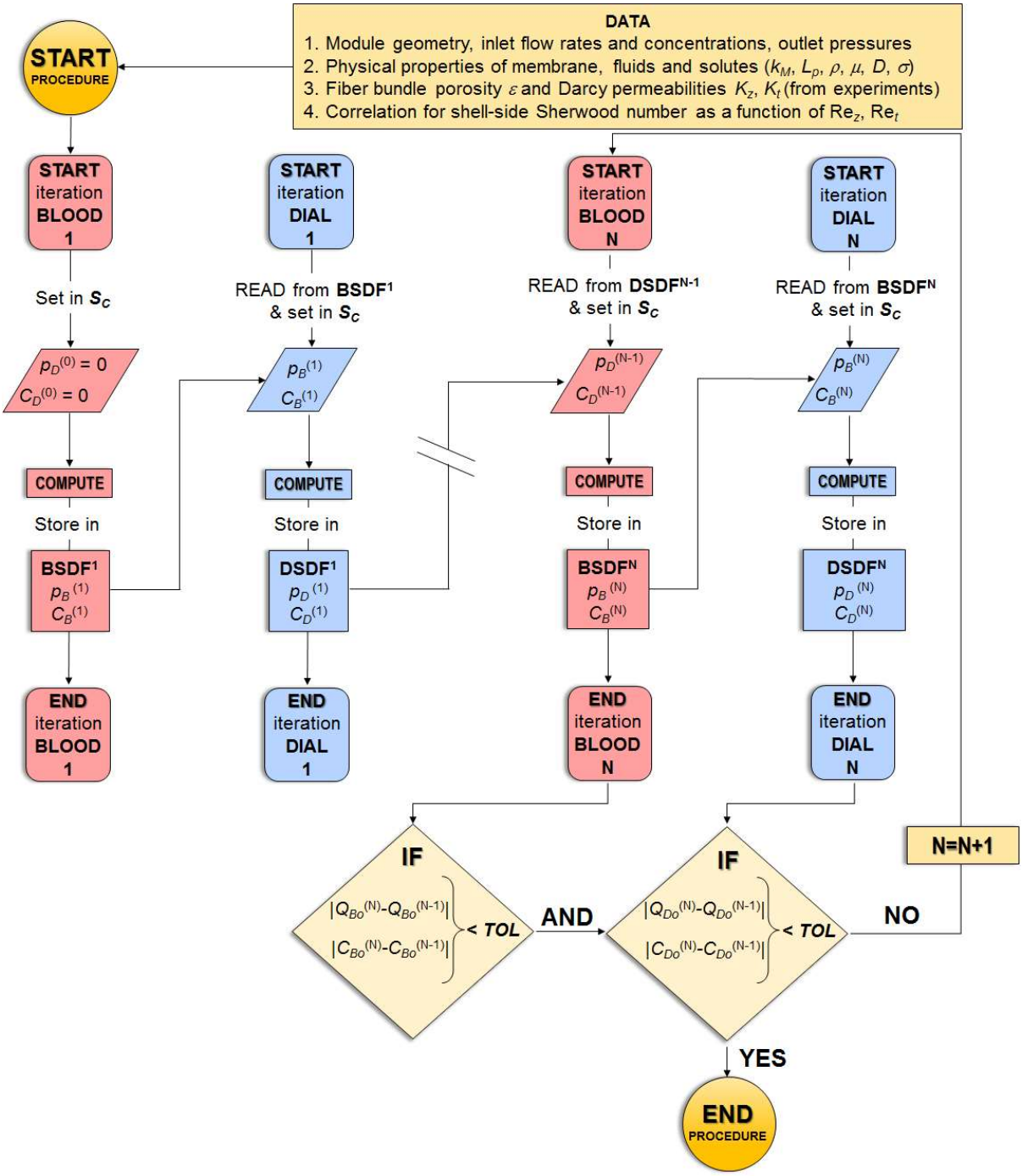


**Figure 9:** Flow chart of the computational process.

# 4. Results and discussion

## 4.1 Grid independence

A grid independence test was conducted for the geometry representative of the PHYLTER® HF 17SD module. The inlet blood flow rate was 300 mL/min and the inlet dialysate flow rate was 500 mL/min. The ultrafiltration flow rate was set at 10 mL/min. Four grids were compared, the total number of finite volumes increasing from ~28,000 to ~890,000 with a

ratio of $\sim\sqrt{10}$ between consecutive grids while the distribution of grid points along the three directions remained the same. The grids were made up of hexahedral volumes only, known to provide more accurate results than tetrahedral or hybrid grids.

To check the grid independence of the results, two quantities were monitored: the solute clearance CL, characterizing mass transfer, and the shell-side pressure drop, characterizing hydrodynamics. A grid of ~280,000 finite volumes (with 10,800 cells in the cross sectional plane) was sufficient to achieve a discrepancy below ~1% on both quantities with respect to the finest grid, the more sensitive quantity being the shell-side pressure drop. Therefore, this grid was chosen for all final simulations.

## 4.2 Model validation and influence of modelling options

### *4.2.1 Validation*

For validation purposes, clearance values predicted by the present model were compared with experimental clearances for urea and B12 vitamin obtained at the Medtronic® laboratories. Experiments, following the test protocol already described in Section 2.5, were performed for PHYLTHER® HF SD15 and SD17 modules using a saline solution instead of blood. Therefore, simulations were carried out by replacing in the lumen side blood with a fluid having the same physical properties as the saline solution used in the experiments and setting the relevant oncotic pressure to zero. The dialysate flow rate was fixed at 500 mL/min while three different lumen-side flow rates (200, 300 and 400 mL/min) were simulated. The ultrafiltration flow rate was fixed to 10 mL/min as in the experiments. Membrane diffusive permeability and hydraulic permeability data were those provided by the company as reported in **Table 7**. For the Darcy permeabilities, as already mentioned, values derived from experiments conducted on the specific fiber bundles had to be used since they differed broadly from CFD predictions obtained for regular fiber arrays with no spacing yarn. The relevant experimental procedure is described in detail in the **Supplement**.

**Figure 10** compares model predictions for the clearances of the two solutes with the experimental data reported in **Table 5**. As expected, clearance increases with the blood flow rate and with the size of the module. In all cases, model predictions lie within the dispersion interval of the experimental data. For both modules and both solutes, the best agreement with the experiments is obtained at the least blood flow rate (200 mL/min). The maximum discrepancy is ~–13 mL/min, obtained for B12 vitamin with the 1.5 $m^2$ module at $Q_B$=400 mL/min.

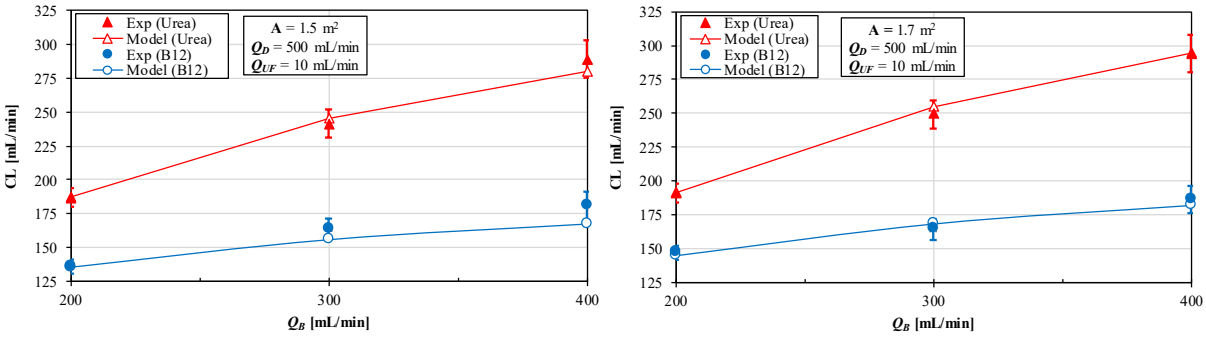


(a) (b)

**Figure 10:** Urea and B12 vitamin clearances as functions of the blood flow rate for the 1.5 $m^2$ (a) and the 1.7 $m^2$ (b) modules: model predictions (solid lines and hollow symbols) are compared with experimental results by Medtronic® (solid symbols). These latter are provided with dispersion bars.

For the two modules, two solutes and three blood flow rates considered for the validation, **Table 9** reports the predicted values of the bulk outlet concentrations both on the blood and on the dialysate sides that satisfy the overall mass balances of each solute and are used to compute the respective clearances. Note that part of this information is redundant since outlet bulk concentrations can be deduced from the corresponding clearances, and is reported here only for the reader's benefit. Experimental clearance values were reported in **Table 5**.

**Table 9:** Predicted bulk outlet concentrations for blood and dialysate used to compute the respective clearances. In all cases, the dialysate inlet flow rate is 500 mL/min, the UF flow rate is 10 mL/min and the inlet concentrations are zero on the dialysate side and 20 mol/$m^3$ (urea) or 0.03 mol/$m^3$ (B12 vitamin) on the blood side.

| Module type | Solute | UREA | | | B12 VITAMIN | | |
|---|---|---|---|---|---|---|---|
| | $Q_{Bi}$ (mL/min) | 200 | 300 | 400 | 200 | 300 | 400 |
| PHYLTER® HF 15SD | $C_{Bo}$ (mol/$m^3$) | 1.26 | 3.79 | 6.15 | $1.03\times10^{-2}$ | $1.49\times10^{-2}$ | $1.78\times10^{-2}$ |
| | $C_{Do}$ (mol/$m^3$) | 7.37 | 9.61 | 10.98 | $7.94\times10^{-3}$ | $9.18\times10^{-3}$ | $9.88\times10^{-3}$ |
| | CL (mL/min) | 188 | 245 | 280 | 135 | 156 | 168 |
| PHYLTER® HF 17SD | $C_{Bo}$ (mol/$m^3$) | 0.84 | 3.10 | 5.44 | $8.84\times10^{-3}$ | $1.37\times10^{-2}$ | $1.68\times10^{-2}$ |
| | $C_{Do}$ (mol/$m^3$) | 7.53 | 10.00 | 11.53 | $8.47\times10^{-3}$ | $9.88\times10^{-3}$ | $1.07\times10^{-2}$ |
| | CL (mL/min) | 192 | 255 | 294 | 144 | 168 | 182 |

### *4.2.2 Influence of the model used for the dialysate-side Sherwood number*

To assess the influence of the model used for the shell side Sherwood number, simulations were carried out for the SD17 module keeping $Sh_D$ fixed at 10, a value close to that for purely axial flow in hexagonal regular lattices at $\varepsilon$=0.51 (9.85). The results for urea are compared

589 with the full model predictions and with the relevant experimental data in **Figure 11**.

590

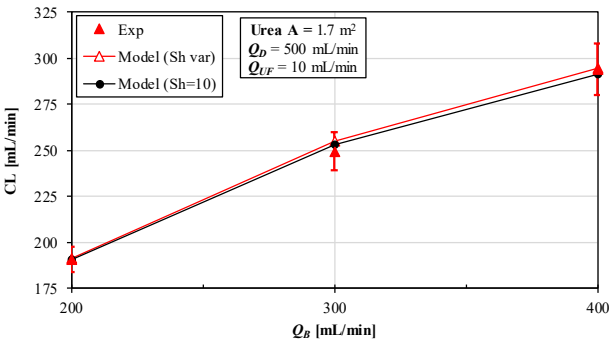


591

592 **Figure 11:** Urea clearance as a function of the blood flow rate for the 1.7 $m^2$ module: predictions
593 obtained by accounting (hollow triangles) or not (solid circles) for the influence of
594 transverse flow on the shell-side Sherwood number are compared with experimental
595 results by Medtronic® (solid triangles).

596

597 The clearances predicted neglecting the influence of transverse flow on $Sh_D$ differ negligibly
598 from those of the full model and fall within the range of dispersion of the experimental data.
599 Therefore, one can state that the model is little sensitive to this option. However, since taking
600 into account a variable value of $Sh_D$ does not significantly affect the computational effort, the
601 full model was preferred in the study.

602

603 *4.2.3 Influence of the model used for the Darcy permeabilities*

604 The impact of the model used for the Darcy permeabilities was also studied. To this purpose,
605 comparative simulations were carried out for the $A$=1.7 $m^2$ module and a lumen side flow rate
606 $Q_B$=300 mL/min using the Darcy permeabilities in **Table 6**, obtained from unit-cell small
607 scale CFD predictions ($K_{z,D}=8.64\times10^{-10}$ $m^2$, $K_{t,D}=3.69\times10^{-10}$ $m^2$, $K_{z,B}=3.58\times10^{-10}$ $m^2$, $K_{t,B}$=0)
608 instead of the corresponding experimental ones in **Table 3** ($K_{z,D}=3.4\times10^{-10}$ $m^2$, $K_{t,D}=3.2\times10^{-11}$
609 $m^2$, $K_{z,B}=3.3\times10^{-10}$ $m^2$, $K_{t,B}$=0).
610 The predictions exhibit a discrepancy of ~0.2% in clearance both for urea and B12 vitamin
611 with respect to the base model. Therefore, as far as mass transfer is concerned, the model
612 proves to be little sensitive to this option. In regard to the flow field, the alternative
613 treatments of permeabilities lead to largely different pressure profiles along the module's
614 length (see **Figure 12**, in which the ultrafiltration flow rate is kept fixed at 10 mL/min).

615

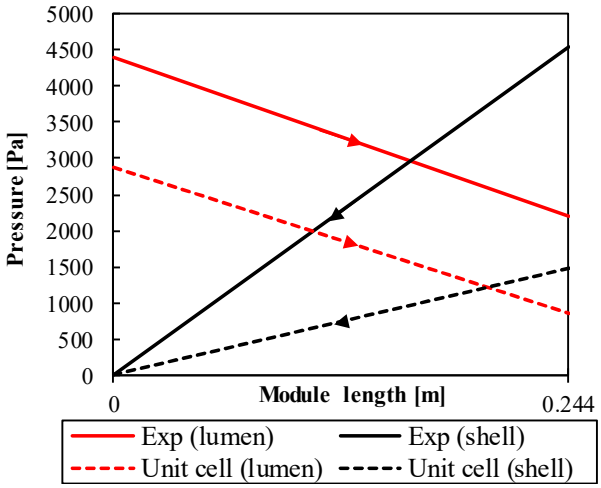


**Figure 12:** Comparison of model predictions for the pressure profiles (red for lumen side, black for shell side) over the length of the hemodialyzer, obtained by using values of Darcy permeabilities from experiment (solid lines) and from small-scale CFD predictions (broken lines). In all cases the ultrafiltration flow rate was kept fixed to 10 mL/min.

**Figure 12** shows that the choice of the model used for the shell-side Darcy permeabilities $K$ significantly affects the slope of the pressure distribution in the dialysate and the pressure levels also in the blood. However, provided the net ultrafiltration rate is kept fixed, almost no influence on mass transfer is obtained: when the CFD-based $K$ values are adopted, the region of back-filtration decreases slightly, while the clearance increases from 254.9 to 255.4 mL/min for urea and decreases from 168.3 to 167.9 mL/min for B12 vitamin.

## 4.3 Detailed results and parametrical sensitivity assessment

Following the above study focussed on the influence of *modelling* options, a parametrical analysis was conducted to assess the sensitivity of the results to different *physical* quantities:

- membrane's diffusive permeability;
- ultrafiltration flow rate;
- lumen-side fluid properties and oncotic pressure;
- dialysate flow rate.

At first, a "base case" was simulated. Then, by changing only one parameter at a time and keeping all other parameters fixed, the influence of its variation on the results was evaluated. This study was performed in the PHYLTER® HF 17SD geometry.

### *4.3.1 Fluid flow and solute concentration distributions for the "base case"*

In the "base case" blood and dialysate flow rates were 300 and 500 mL/min, respectively; the

ultrafiltration flow rate was set to 10 mL/min. Membrane and fluids properties were those summarized in **Table 7** and **Table 8**, respectively. An oncotic pressure of 3700 Pa (~28 mmHg as in typical human blood [39]) was set in the blood. For this "base case" the model predicts for urea and B12 vitamin clearances of ~257 and ~172 mL/min, respectively.

**Figure 13** shows a vector plot of the dialysate velocity in a *xy* cross section near the dialysate outlet end of the module.

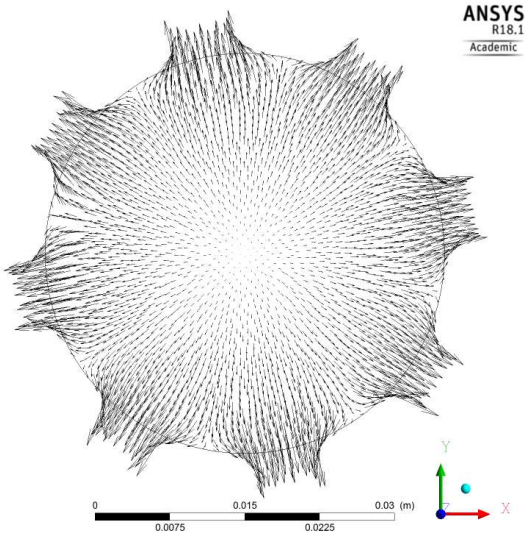


**Figure 13:** Vector plot of the shell (dialysate) fluid flow near the outlet of the module.

The fluid flow, almost everywhere parallel to the fiber bundle, is subjected to a change of direction from the middle to the periphery of the module in the end regions, yielding significant values of the cross-flow velocity $u_t$.

Pressure distributions in both compartments of the module are reported in **Figure 14**(a, b). Blood flows from right to left while dialysate flows from left to right.

The maps show, both on the blood and on the dialysate sides, a linear pressure gradient over most the module's length, a trend similar to that reported by Osuga *et al.* [40]. Inlet-outlet pressure drops were ~9860 Pa in the blood and ~4400 Pa in the dialysate. This difference is due to the difference both in the physical properties of the two fluids, the blood being ~5 times more viscous than the dialysate (see **Table 8**), and in the relevant axial Darcy permeabilities. The blood outlet pressure was adjusted to 2156 Pa so as to obtain an ultrafiltration flow rate of 10 mL/min.

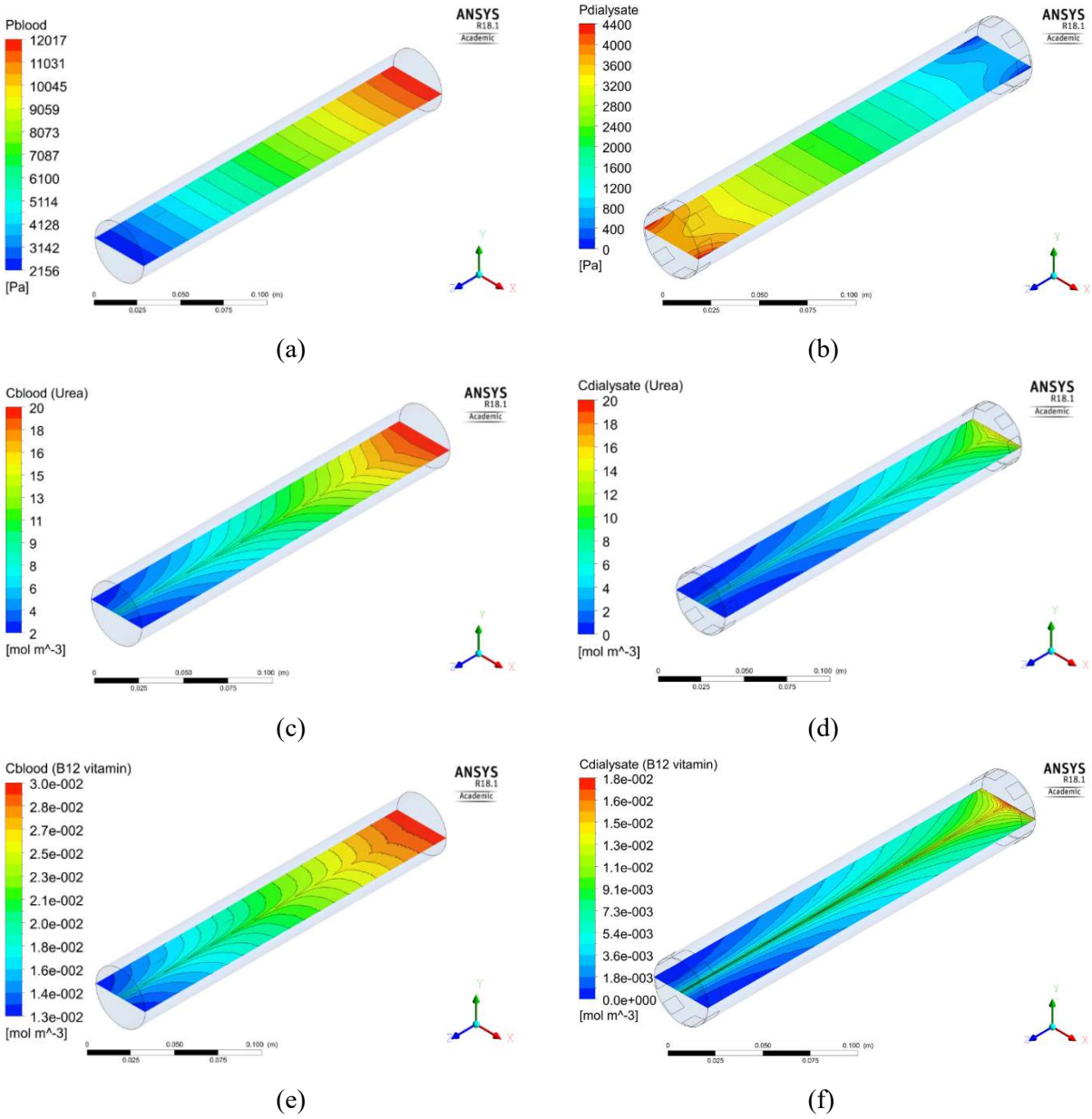


**Figure 14:** False-color maps of pressure and solute concentration in the *zx* mid-plane. Left column: lumen (blood) side; right column: shell (dialysate) side. (a), (b): pressure; (c), (d): concentration of urea; (e), (f): concentration of B12 vitamin.

Corresponding distributions of urea and B12 vitamin concentrations are reported in **Figure 14**(c)-(f). The maps exhibit a mainly axial concentration stratification both in the blood and in the dialysate, superimposed on a radial gradient which is largest in the regions corresponding to dialysate inlet / blood outlet and is caused by the peripheral locations of the dialysate inlet-outlet ports. These results are qualitatively similar to those reported by Ding *et al*. [25].

Flow and concentration fields in the dialysate outlet region of the module are shown in greater detail in **Figure 15**. The main map reports predicted dialysate streamlines and urea concentration distribution in a plane containing the module's axis and bisecting two outlet

openings. Here, the dialysate flow is from right to left and some of the eight outlet openings are outlined. The smaller maps on the left report the distributions of normal (radial) outlet velocity and solute concentration in a generic outlet opening.

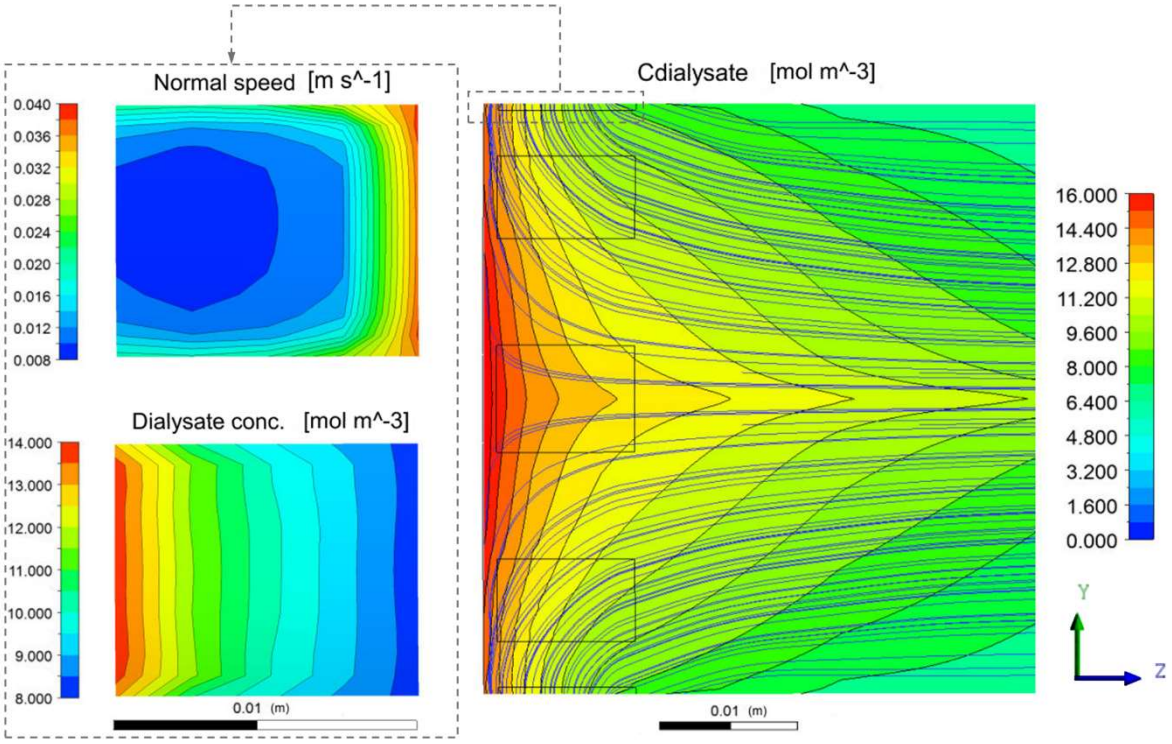


**Figure 15:** Main map: streamlines and solute concentration distribution in a plane containing the axis and bisecting two outlet openings (dialysate flow is from right to left; some of the eight outlet openings are outlined). The small maps on the left show the distributions of normal (radial) outlet velocity and solute concentration in a generic outlet opening.

It can be observed that the fluid stagnates against the flat left end of the module, where the solute concentration attains very high values (~16 mol/m$^3$). On the other hand, the fluid exiting (radially) the outlet ports carries a lower solute concentration; as shown in the relevant detail on the left, this ranges from ~8 to ~14 mol/m$^3$, with an area-averaged value of ~10.4 mol/m$^3$. Moreover, the normal outlet velocity exhibits an opposite distribution, so that the mass flow averaged (bulk) solute concentration in the fluid leaving the module is even lower (~10.1 mol/m$^3$). This last figure is the concentration value that closes mass balances and allows the correct computation of the solute clearance (257 mL/min).

### *4.3.2 Influence of the membrane's diffusive permeability*

The first parameter investigated was the membrane's diffusive permeability $k_M$. In the light of Eq. (10) and **Figure 7**, this parameter heavily affects the overall mass transfer coefficient $U$,

being $(k_M)^{-1}$ the largest contribution to diffusive mass transfer resistance.

The effects of $k_M$ on the results were studied by setting membrane's diffusive permeabilities doubled ($2.2\times10^{-5}$ m/s for urea, $6.2\times10^{-6}$ m/s for B12 vitamin) and halved ($0.55\times10^{-5}$ m/s for urea, $1.55\times10^{-6}$ m/s for B12 vitamin) with respect to the values used in the "base case". No other parameters were changed. **Figure 16** reports mass flow averaged (i.e., bulk) solute concentrations in blood and dialysate, computed on cross sections of the module as functions of the axial location. Graph (a) is for urea, graph (b) for B12 vitamin, and the three curves reported for each quantity are for the three values of $k_M$ examined.

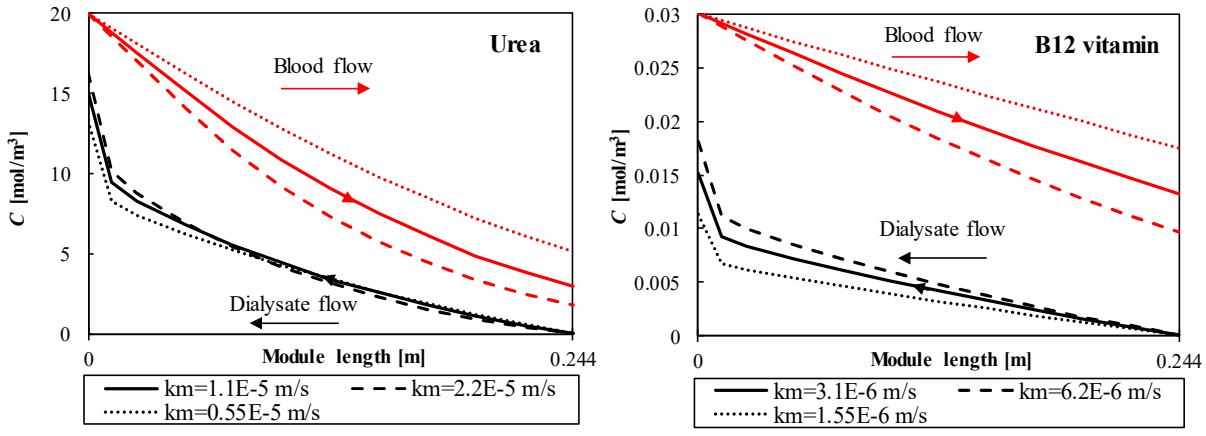


(a) (b)

**Figure 16:** Solute bulk concentration profiles for urea (a) and B12 vitamin (b) both in blood (red lines) and in dialysate (black lines) as functions of the axial coordinate. Profiles are for $k_M$ values provided by Medtronic® (solid lines); doubled values of $k_M$ (broken lines); halved values of $k_M$ (dotted lines).

Note that in the dialysate the bulk concentrations at $z=L$ (dialysate inlet end of the module) and $z=0$ (dialysate outlet end of the module) reported in **Figure 16** do *not* coincide with the inlet and outlet bulk concentrations for the reasons discussed above. In particular, the dialysate outlet end region of the module is filled with practically stagnant fluid whose concentration attains very high values (e.g. ~0.016 mol/m$^3$ for B12 vitamin in the base case $k_M=3.1\times10^{-6}$ m/s), explaining the sharp concentration rise in the proximity of the dialysate outlet. The corresponding bulk outlet concentration (not shown in the plots) is much lower (~0.010 mol/m$^3$ for the same case).

Plots of mean concentration of a solute in the dialysate along the module's length which strongly resemble our results in **Figure 16** have been reported by Ding *et al.* [25]. In particular, they exhibit the same sharp increase near the end of the module and are explained by the authors by the same mechanism (fluid stagnation caused by the outlet port geometry).

Contrariwise, in the blood (which enters and exits the module in axial flow) the maximum and minimum concentrations reported in **Figure 16** coincide with the bulk inlet and outlet concentrations, respectively.

The results of the parametrical study are the expected ones. Consider, for example, the case of B12 vitamin in **Figure 16**(b). In the "base case", the blood solute concentration at $z$=0 (blood inlet end of the module) is $3\times10^{-2}$ mol/m$^3$ and decreases to ~$1.3\times10^{-2}$ mol/m$^3$ at $z$=$L$ (blood outlet end of the module). The two cases involving doubled and halved values of $k_M$ lead to blood solute concentrations at $z$=$L$ of ~$1.0\times10^{-2}$ and ~$1.75\times10^{-2}$mol/m$^3$, respectively. Similar considerations apply also to urea.

Changes in concentrations imply changes in solute clearances, which increase from ~257 to ~275 mL/min (urea) and from ~172 to ~207 mL/min (B12 vitamin) when $k_M$ values are doubled, while they decrease to ~225 mL/min (urea) and ~130 mL/min (B12 vitamin) when they are halved. Thus, concentrations and clearance are highly sensitive to $k_M$ variations.

Since $k_M$ is an uncertainty-affected parameter, the uncertainty on $k_M$ reflects in an uncertainty on clearance, which was better assessed by conducting further comparative simulations in which $k_M$ was made to vary by a small amount. For urea, the relative uncertainty on $k_M$ of ±18% reported in **Table 7** translates into an uncertainty of ±1.6% in the predicted clearance. For B12 vitamin the relative uncertainty of ±6.5% reported in **Table 7** translates into an uncertainty of the predicted clearance of ±2%.

### *4.3.3 Influence of the ultrafiltration flow rate*

The effect of the ultrafiltration flow rate $Q_{UF}$ on the model's predictions was also studied. Keeping all other model parameters fixed at the "base case" values, the simulations were repeated for $Q_{UF}$=0 and $Q_{UF}$=20 mL/min. Since the convective term of the solute's scalar transport equation has only a minor influence in a hemodialysis process, mass transfer predictions are expected to be little sensitive to this parameter.

**Figure 17** shows bulk concentrations of urea and B12 vitamin in blood and dialysate. As in **Figure 16**, these quantities are reported as functions of the axial coordinate $z$.

There are only slight differences in the concentration profiles, so that noticeable changes from the "base case" are not expected in terms of solute clearance. In fact, clearance values increase from ~257 mL/min for urea and ~172 mL/min for B12 vitamin ("base case" at $Q_{UF}$=10 mL/min) to ~260 and ~178 mL/min, respectively, when $Q_{UF}$=20 mL/min and decrease to ~254 and ~167 mL/min, respectively, when $Q_{UF}$=0.

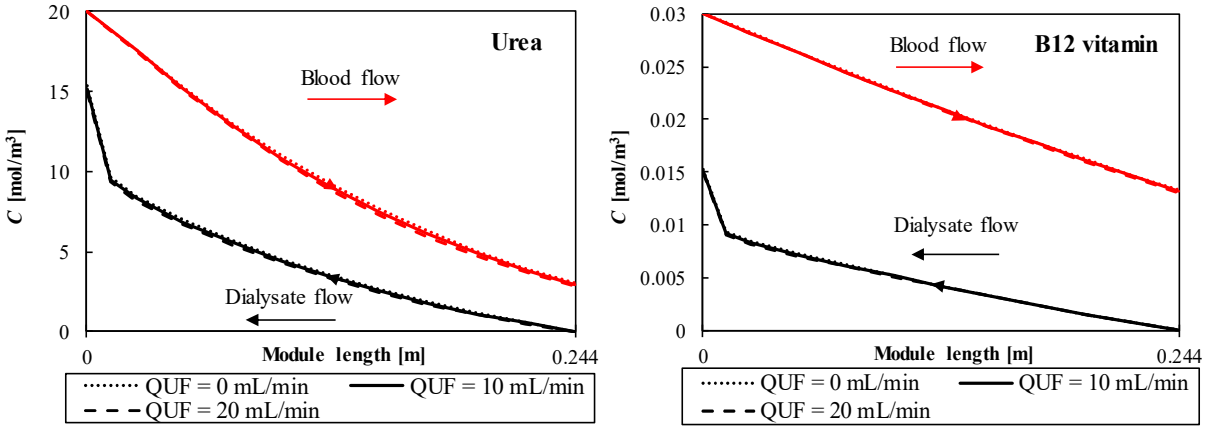


(a) (b)

**Figure 17:** Solute bulk concentration profiles for urea (a) and B12 vitamin (b) both in blood (red lines) and in dialysate (black lines) as functions of the axial coordinate. Profiles are for $Q_{UF}$=10 mL/min (solid lines), 20 mL/min (broken lines) and 0 (dotted lines).

Different considerations apply to the influence of $Q_{UF}$ on hydrodynamics. By changing $Q_{UF}$, the pressures diagrams change as shown in **Figure 18**. As $Q_{UF}$ increases, the blood pressure curve preserves its slope but is shifted towards higher pressures, and the extent of the back-filtration region decreases. Therefore, the influence of $Q_{UF}$ on hydrodynamics is not negligible and directly affects the nature of the treatment, turning it from a pure hemodialysis process into a hemodiafiltration one.

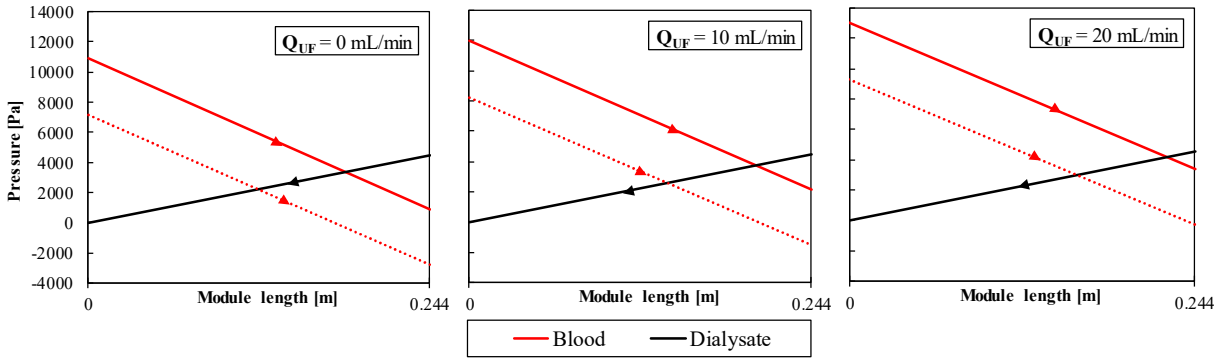


(a) (b) (c)

**Figure 18:** Pressure profiles over the length of the hemodialyzer in blood (red lines) and dialysate (black lines) for $Q_{UF}$=0 (a), 10 mL/min (b), 20 mL/min (c). For the blood, solid lines correspond to pressure, dotted lines to pressure minus oncotic pressure.

### *4.3.4 Influence of the physical properties of the lumen-side fluid*

The influence of the physical properties of the lumen-side fluid was studied by comparing the

"base case" with a simulation in which, in the lumen side, blood was replaced by saline water as in clearance measurements.

In **Figure 19**, graph (a) compares axial profiles of lumen- and dialysate-side pressures while graph (b) compares axial profiles of the solution ultrafiltration flux:

$$q_{UF} = L_p \cdot (p_B - p_D - p_{onc}) \tag{13}$$

(expressed in m $s^{-1}$), in which $L_p$, $p_B$, $p_D$ and $p_{onc}$ were defined in Section 3.3.

Replacing blood with saline water reduces the slope of the lumen-side pressure because of the lower viscosity of water with respect to blood, while leaving the shell-side (dialysate) pressure profile unchanged. Thus, the average trans-membrane pressure decreases from ~4800 to ~1100 Pa. However, when the lumen-side fluid is blood, an oncotic pressure of ~3700 Pa (~28 mmHg as already mentioned) must be subtracted from its pressure, yielding an effective trans-membrane pressure of ~1100 Pa as in the saline water case, so that the overall ultrafiltration rate $Q_{UF}$ remains fixed to the chosen reference value of 10 mL/min. The axial profile of its local rate, $q_{UF}$, however, does change as shown by **Figure 19**(b).

In their turn, changes in $q_{UF}$ affect the distribution of the local *solute* ultrafiltration flux $J_{UF}$:

$$J_{UF} = q_{UF} \cdot C_{s,M} \cdot (1 - \sigma) \tag{14}$$

(expressed in mol $m^{-2}$ $s^{-1}$), in which $C_{s,M}=(C_B+C_D)/2$, see Eq. (9.b).

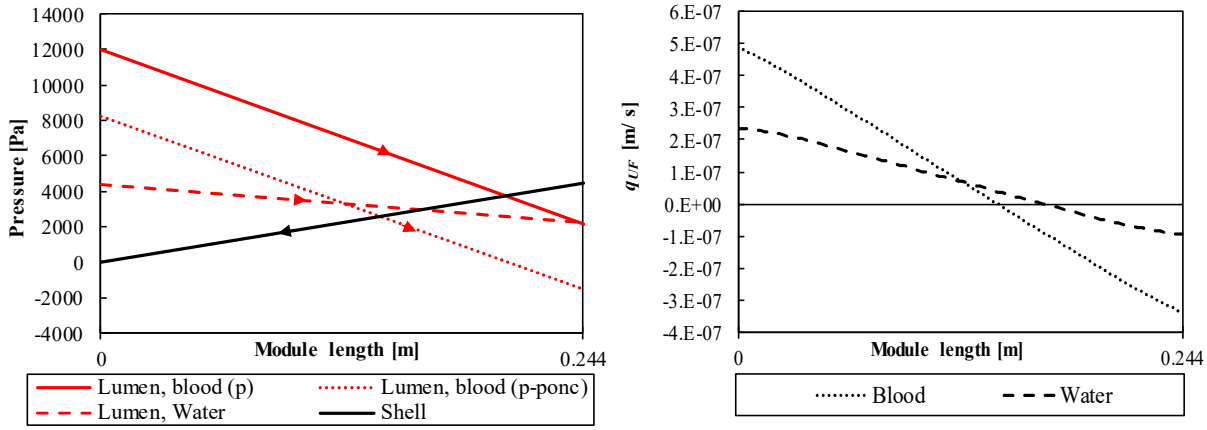


(a) (b)

**Figure 19:** (a) Axial pressure profiles in lumen (red lines) and shell (black line) for lumen fed with blood or with a saline water solution. Red solid line: pressure, feed=blood; red dotted line: pressure minus oncotic pressure, feed=blood; broken line: pressure, feed=saline water. (b) Axial profiles of solution ultrafiltration flux on the module's axis for lumen fed with blood (dotted line) or with saline water (broken line).

As an example, **Figure 20** reports profiles of $J_{UF}$, evaluated on the module's longitudinal axis for urea (a) and B12 vitamin (b), over the length of the hemodialyzer.

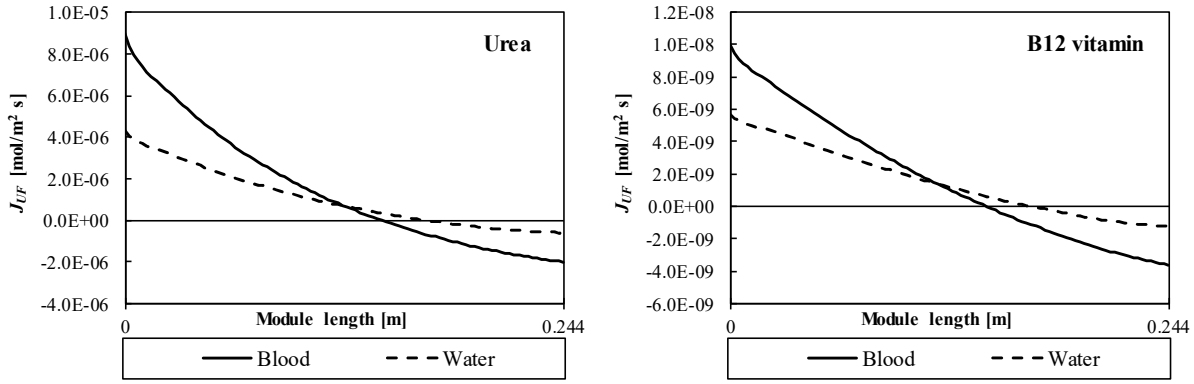


(a) (b)

**Figure 20:** Profiles of solute ultrafiltration flux over the length of the hemodialyzer for lumen fed with either blood (solid lines) or saline water solution (broken lines). (a): urea; (b): B12 vitamin.

The distribution of $J_{UF}$ behaves as that of $q_{UF}$ in **Figure 19**(b), and is clearly affected by the lumen-side fluid's properties. However, when blood is replaced by saline water, $J_{UF}$ decreases in absolute value both in the forward-filtration region (left region in the plots) and in the back-filtration one (right region in the plots). Its volume integral changes little and so does clearance, which decreases from ~257 mL/min to ~255 mL/min for urea and from ~172 mL/min to ~168 mL/min for B12 vitamin.

### *4.3.5 Influence of the dialysate flow rate*

Also the variation of the dialysate flow rate $Q_D$ obviously affects the results in terms of solute clearance. **Figure 21** reports profiles of urea and B12 vitamin bulk concentrations along the length of the hemodialyzer, as computed for $Q_D$=500 mL/min ("base case" value) or 750 mL/min, while $Q_B$ is kept fixed at 300 mL/min.

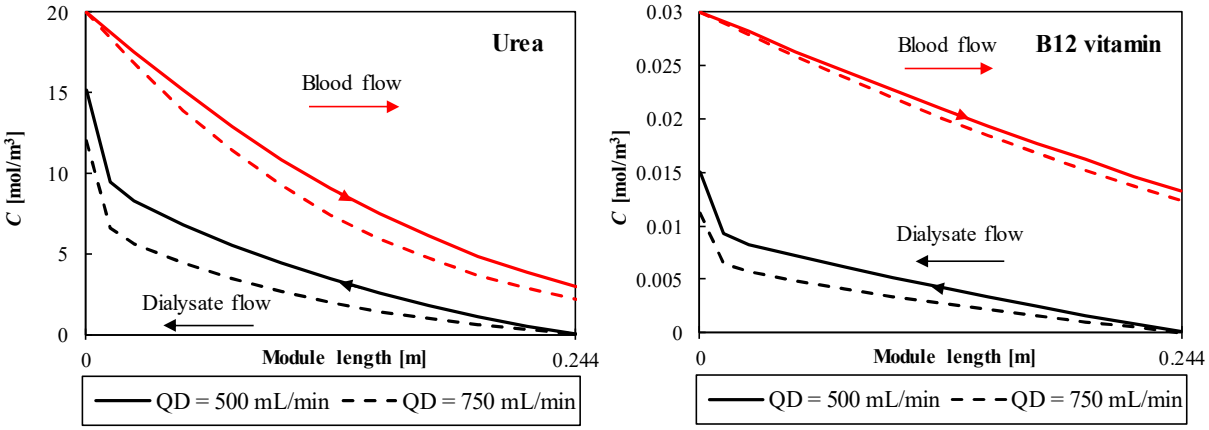


(a) (b)

**Figure 21:** Solute bulk concentration profiles for urea (a) and B12 vitamin (b) both in blood (red lines) and in dialysate (black lines) as functions of the axial coordinate. Profiles correspond to $Q_D$=500 mL/min (solid lines) and $Q_D$=750 mL/min (broken lines).

Increasing $Q_D$ causes the concentrations to decrease significantly on both sides and for both solutes, while the concentration difference, and thus the solute flux, increases. In particular, the concentration in blood at $z=L$ (blood outlet end of the dialyzer) decreases from 2.96 to 2.15 mol/m$^3$ for urea and from $1.32\cdot10^{-2}$ to $1.24\cdot10^{-2}$ mol/m$^3$ for B12 vitamin. Correspondingly, the clearance increases from ~257 to ~269 mL/min for urea and from ~172 to ~180 mL/min for B12 vitamin.

### *4.3.6 Summary of the parametrical study*

**Figure 22** summarizes, in terms of solute clearance, the results of the parametrical study discussed in the previous Sections.

For each solute, i.e. urea (a) and B12 vitamin (b), the "base case" result is represented by the red bar, while the other bars correspond to each of the variants analyzed above.

The most effective parameter is the membrane's diffusive permeability, for which doubling $k_M$ leads to an enhancement in clearance of ~18 mL/min for urea and of ~35 mL/min for B12 vitamin, while halving $k_M$ yields a decrease in clearance of ~32 mL/min for urea and ~42 mL/min for B12 vitamin.

The second most effective parameter is the dialysate flow rate $Q_D$. When $Q_D$ varies from 500 to 750 mL/min the clearance increases by ~12 and ~8 mL/min for urea and B12 vitamin, respectively.

A minor effect on clearance is associated with the variation of the ultrafiltration flow rate $Q_{UF}$, despite the significant influence of this parameter on hydrodynamics (notably back-

filtration), already pointed out in Section 4.3.3. Setting $Q_{UF}$=0 mL/min led to a small decrease of the clearance (~3 mL/min for urea and ~5 mL/min for B12 vitamin) in comparison with the "base case"; setting $Q_{UF}$=20 mL/min yielded a weak clearance enhancement (~3 mL/min for urea and ~6 mL/min for B12 vitamin).

Finally, the parameter that has the least influence on the solute clearance is the oncotic pressure; a negligible effect was obtained for both solutes by accounting or not for the presence of plasma proteins in the blood.

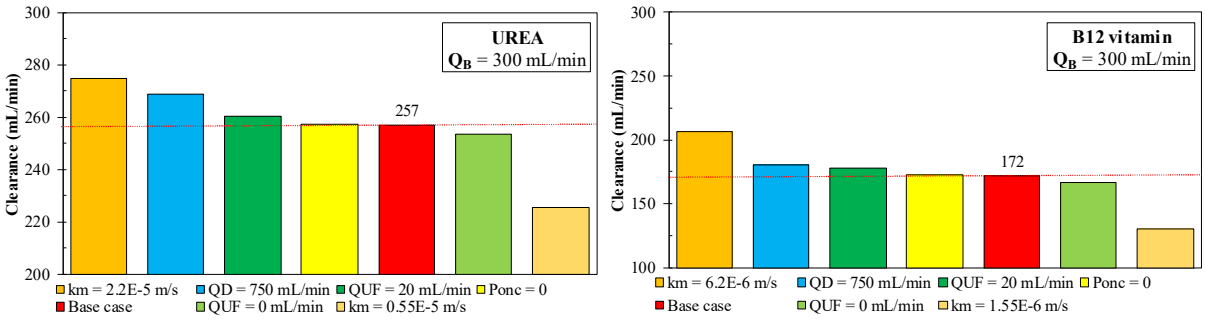


(a) (b)

**Figure 22:** Summary of the solute clearances obtained in the parametrical analysis for urea (a) and B12 vitamin (b).

## Conclusions

Destructive tests conducted on actual hemodialysis modules provided information on porosity, number of fibers, fiber internal and external diameters, and bundle structure. The bundle porosity was consistent with the nominal values reported by the manufacturer. Fiber diameters and thickness exhibited a significant amount of statistical dispersion. A noteworthy feature of the bundles analyzed was the presence of yarn filaments, grouped in tufts interspersed between the hollow fibers. The yarn caused the arrangement of the fibers over the generic cross section of a module to depart from a truly random distribution and to exhibit large-scale clustering, with regions of high porosity alternating with more compact zones.

Axial and transverse Darcy permeabilities of the bundles were measured. On the blood side, the axial permeability agreed well with that derived for Hagen-Poiseuille flow. On the shell-side, the experimental values were ~2.5 times (axial) and ~11 times (transverse) lower than CFD predictions for flow around regular hexagonal cylinder arrays. Most of this large discrepancy can be explained by the presence of the spacing yarn, which makes experimental values of the shell-side permeabilities necessary for a correct prediction of pressure distributions in a hemodialyzer, which, in its turn, affect flow patterns and ultrafiltration

rates.

The bundles' hydraulic and mass transfer properties, obtained by combining the above experimental results with theoretical considerations and CFD predictions, were then fed to a porous-media model of a hemodialyzer.

The model was first validated against experimental clearance data. Computational results fell within the dispersion range of the experiments; the increase of clearance with the lumen-side flow rate and the module size was correctly predicted.

A parametrical study on the influence of different physical quantities and operating conditions showed that clearance is affected, in decreasing order of significance, by the membrane's diffusive permeability, the dialysate flow rate and the ultrafiltration flow rate. The oncotic pressure in blood has a negligible influence. Therefore, the room for performance improvements, at least in terms of clearance, is closely related to the appearance on the stage of a novel generation of membranes exhibiting a significantly larger diffusive permeability.

The modelling approach developed here is quite general and can be applied not only to hemodialysis but (with the appropriate modifications) also to other processes characterized by heat or mass transfer between two segregated fluids.

## Acknowledgments

Part of this work was carried out with the financial support of the *Programma Operativo Nazionale Ricerca e Innovazione 2014-2020 (CCI 2014IT16M2OP005), Fondo Sociale Europeo, Azione I.1 "Dottorati Innovativi con caratterizzazione Industriale"*.

## Nomenclature

| | |
|---|---|
| $A$ | nominal internal area of the hemodialyzer ($m^2$) |
| $A_{af}$ | cross sectional area of the bundle in axial flow condition ($m^2$) |
| $A_{cf}$ | cross sectional area of the bundle in cross flow condition ($m^2$) |
| $A_{ext}$ | total external area of the hollow fibers ($m^2$) |
| $a$, $b$, $c$ | parameters in $Sh_D$ – $Re_t$ correlation (-) |
| $C$ | solute concentration (mol $m^{-3}$) |
| CL | solute clearance (mL/min) |
| $D$ | solute diffusion coefficient ($m^2$ $s^{-1}$) |
| $D_i$ | inner diameter of the module (m) |

| | | |
|---|---|---|
| 932 | $d_e$ | outer diameter of the fiber m) |
| 933 | $d_h$ | hydraulic diameter (m) |
| 934 | $d_i$ | inner (lumen) diameter of the fiber (m) |
| 935 | $J$ | local mass flux at the wall (mol $m^{-2}$ $s^{-1}$) |
| 936 | $k$ | mass transport coefficient (m $s^{-1}$) |
| 937 | $K$ | Darcy permeability based on the superficial velocity ($m^2$) |
| 938 | $K'$ | Darcy permeability based on the interstitial velocity ($m^2$) |
| 939 | $L$ | effective length of the fibers (m) |
| 940 | $L_p$ | membrane hydraulic permeability (m $s^{-1}$ $Pa^{-1}$) |
| 941 | $N_0$ | nominal number of the fibers (-) |
| 942 | $p$ | pressure (Pa) |
| 943 | $q$ | specific flow rate (m/s) |
| 944 | $Q$ | flow rate (mL/min) |
| 945 | $R$ | hydraulic resistance (Pa s $m^{-3}$) |
| 946 | Re | Reynolds number (-) |
| 947 | $s$ | membrane thickness (m) |
| 948 | $S_C$ | source term for the solute transport equation (mol $m^{-3}$ $s^{-1}$) |
| 949 | $S_M$ | source term for the momentum equations (Pa $m^{-1}$) |
| 950 | Sc | Schmidt number (-) |
| 951 | Sh | Sherwood number (-) |
| 952 | $t$ | cross-flow direction (m) |
| 953 | $U$ | overall mass transfer coefficient (m $s^{-1}$) |
| 954 | $\vec{u}$ | velocity vector (m $s^{-1}$) |
| 955 | $V$ | volume ($m^3$) |
| 956 | $x, y$ | Cartesian coordinates in cross section orthogonal to the fibers (m) |
| 957 | $z$ | Cartesian coordinate parallel to the fibers (m) |
| 958 | | |
| 959 | **Greek symbols** | |
| 960 | $\Delta p$ | pressure drop (Pa) |
| 961 | $\varepsilon$ | porosity (-) |
| 962 | $\mu$ | dynamic viscosity (Pa s) |
| 963 | $\rho$ | density (kg $m^{-3}$) |
| 964 | $\sigma$ | Staverman's reflection coefficient (-) |

| | | |
|---|---|---|
| $\sigma_{CL}$ | standard deviation for clearance experimental data (mL/min) |

**Subscripts**

| | |
|---|---|
| *af* | axial flow |
| *avg* | average |
| *bulk* | bulk (mass flow averaged) |
| *B* | blood (lumen side) |
| *cf* | cross flow |
| *D* | dialysate (shell side) |
| *DEV* | development |
| *ext* | external |
| *f* | fluid |
| *i* | inlet |
| *M* | membrane |
| *o* | outlet |
| *onc* | oncotic |
| *s* | solute |
| *t* | transverse (lying in a plane orthogonal to the fibers) |
| *tot* | total |
| *UF* | ultrafiltration |
| *wall* | wall (external surface of the fibers) |
| *x*, *y*, *z* | coordinates |
| 1, 2 | compartment number in the 1-D hydrodynamic model |

**Averages**

| | |
|---|---|
| $\bar{\ }$ | surface average |
| $\langle\ \rangle$ | volume average |

**Acronyms**

| | |
|---|---|
| CFD | Computational Fluid Dynamics |
| MW | Molecular Weight |
| UF | Ultrafiltration |

# References


[1] K.J. Jager, C. Kovesdy, R. Langham, M. Rosenberg, V. Jha, C. Zoccali, A single number for advocacy and communication-worldwide more than 850 million individuals have kidney diseases, Nephrol. Dial. Transplant. 34 (2019) 1803–1805. https://doi.org/10.1093/ndt/gfz174.

[2] United States Renal Data System, 2018 USRDS annual data report: Epidemiology of kidney disease in the United States. National Institutes of Health, National Institute of Diabetes and Digestive and Kidney Diseases, Bethesda, MD, 2018, n.d.

[3] Dialysis Market Size, Share & COVID-19 Impact Analysis, By Type (Products and Services), By Dialysis Type (Hemodialysis and Peritoneal Dialysis), By End User (Dialysis Centers & Hospitals and Home Care), and Regional Forecast, 2020-2027; Jun, 2020., n.d.

[4] F. Villarroel, E. Klein, F. Holland, Solute flux in hemodialysis and hemofiltration membranes, Trans. Am. Soc. Artif. Intern. Organs. 23 (1977) 225–232.

[5] Y.L. Chang, C.J. Lee, Solute transport characteristics in hemodiafiltration, J. Memb. Sci. 39 (1988) 99–111.

[6] S.M. Ross, D.A. Uvelli, A.L. Babb, One-Dimensional Mathematical Model of Transmembrane Diffusional and Convective Mass Transfer in a Hemodialyzer, Am. Soc. Mech. Eng. (1973) 8.

[7] C. Legallais, G. Catapano, B. Von Harten, U. Baurmeister, A theoretical model to predict the in vitro performance of hemodiafilters, J. Memb. Sci. 168 (2000) 3–15.

[8] C. Gostoli, A. Gatta, Mass transfer in a hollow fiber dialyzer, J. Memb. Sci. 6 (1980) 133–148.

[9] H. Hamid, J. Mohammad, F. Sobhani, Modelling of Blood and Dialysate Flow in Hollow-Fiber Hemodialyzers, J. Bioeng. Biomed. Sci. 08 (2018) 8–11.

[10] M.Y. Jaffrin, L. Ding, J.M. Laurent, Simultaneous Convective and Diffusive Mass Transfers in a Hemodialyser, J. Biomech. Eng. 112 (1990) 212–219.

[11] H.E. Abaci, S.A. Altinkaya, Modeling of hemodialysis operation, Ann. Biomed. Eng. 38 (2010) 3347–3362.

[12] D. Donato, A. Boschetti-de-Fierro, C. Zweigart, M. Kolb, S. Eloot, M. Storr, B. Krause, K. Leypoldt, P. Segers, Optimization of dialyzer design to maximize solute removal with a two- dimensional transport model, J. Memb. Sci. 541 (2017) 519–528.

[13] K.B. Lim, P.C. Wang, H. An, S.C.M. Yu, Computational Studies for the Design

Parameters of Hollow Fibre Membrane Modules, J. Memb. Sci. 529 (2017) 263–273. https://doi.org/10.1016/j.memsci.2017.01.053.

[14] N. Cancilla, L. Gurreri, G. Marotta, M. Ciofalo, A. Cipollina, A. Tamburini, G. Micale, CFD prediction of shell-side flow and mass transfer in regular fiber arrays, Int. J. Heat Mass Transf. 168 (2021) 120855.

[15] S. Eloot, D. De Wachter, I. Van Tricht, P. Verdonck, Computational flow modeling in hollow-fiber dialyzers, Artif. Organs. 26 (2002) 590–599. https://doi.org/10.1046/j.1525-1594.2002.07081.x.

[16] C. Ma, Y. Liu, F. Li, C. Shen, M. Huang, Z. Wang, C. Cao, Q. Zhou, Y. Sheng, W. Sand, CFD simulations of fiber-fiber interaction in a hollow fiber membrane bundle: Fiber distance and position matters, Sep. Purif. Technol. 209 (2019) 707–713. https://doi.org/10.1016/j.seppur.2018.09.029.

[17] J. Lemanski, G.G. Lipscomb, Effect of shell-side flows on hollow-fiber membrane device performance, AIChE J. 41 (1995) 2322–2326.

[18] J. Happel, H. Brenner, Low Reynolds number hydrodynamics, Prentice-Hall, Englewood Cliffs, 1965. https://doi.org/10.1017/cbo9781316134030.008.

[19] L. Skartsis, J.L. Kardos, B. Khomami, Resin flow through fiber beds during composite manufacturing processes. Part I: Review of newtonian flow through fiber beds, Polym. Eng. Sci. 32 (1992) 221–230. https://doi.org/10.1002/pen.760320402.

[20] Z. Liao, C.K. Poh, Z. Huang, P.A. Hardy, W.R. Clark, D. Gao, A Numerical and Experimental Study of Mass Transfer in the Artificial Kidney, J. Biomech. Eng. 125 (2003) 472.

[21] S. Eloot, Y. D'Asseler, P. De Bondt, P. Verdonck, Combining SPECT medical imaging and computational fluid dynamics for analyzing blood and dialysate flow in hemodialyzers, Int. J. Artif. Organs. 28 (2005) 739–749.

[22] M. Łabęcki, J.M. Piret, B.D. Bowen, Two-dimensional analysis of fluid flow in hollow-fibre modules, Chem. Eng. Sci. 50 (1995) 3369–3384. https://doi.org/10.1016/0009-2509(95)00185-8.

[23] J. Lemanski, G.G. Lipscomb, Effect of shell-side flows on the performance of hollow-fiber gas separation modules, J. Memb. Sci. 195 (2002) 215–228.

[24] W. Ding, L. He, G. Zhao, H. Zhang, Z. Shu, D. Gao, Double porous media model for mass transfer of hemodialyzers, Int. J. Heat Mass Transf. 47 (2004) 4849–4855. https://doi.org/10.1016/j.ijheatmasstransfer.2004.04.017.

[25] W. Ding, W. Li, S. Sun, X. Zhou, P.A. Hardy, S. Ahmad, D. Gao, Three-Dimensional

Simulation of Mass Transfer in Artificial Kidneys, Artif. Organs. 39 (2015) E79–E89.
[26] A. Frank, G.G. Lipscomb, M. Dennis, Visualization of concentration fields in hemodialyzers by computed tomography, J. Memb. Sci. 175 (2000) 239–251. https://doi.org/10.1016/S0376-7388(00)00421-X.
[27] A. Frank, G.G. Lipscomb, M. Dennis, Visualizing the entrapment of air pockets in the shell of a hemodialyzer during wet-out, Chem. Eng. Commun. 184 (2001) 139–155. https://doi.org/10.1080/00986440108912845.
[28] T. Bergman, A. Lavine, F. Incropera, D. Dewitt, Fundamentals of Heat and Mass Transfer, 7th ed., John Wiley & Sons, 2011.
[29] M. Ciofalo, M. Di Liberto, L. Gurreri, M. La Cerva, L. Scelsi, G. Micale, Mass transfer in ducts with transpiring walls, Int. J. Heat Mass Transf. 132 (2019) 1074–1086. https://doi.org/10.1016/j.ijheatmasstransfer.2018.12.059.
[30] Z. Liao, E. Klein, C.K. Poh, Z. Huang, J. Lu, P.A. Hardy, D. Gao, Measurement of hollow fiber membrane transport properties in hemodialyzers, J. Memb. Sci. 256 (2005) 176–183. https://doi.org/10.1016/j.memsci.2005.02.032.
[31] S. Middleman, Transport phenomena in the cardiovascular system, Wiley-Interscience series on biomedical engineering, Wiley-Interscience, 1972.
[32] D.W. Green, R.H. Perry, Perry's Chemical Engineers' Handbook, 8th ed., McGraw-Hill, New York, 2008.
[33] E. Klein, F. Holland, A. Lebeouf, A. Donnaud, J.K. Smith, Transport and mechanical properties of hemodialysis hollow fibers, J. Memb. Sci. 1 (1976) 371–396. https://doi.org/10.1016/S0376-7388(00)82283-8.
[34] K.E. Dionne, B.M. Cain, R.H. Li, W.J. Bell, E.J. Doherty, D.H. Rein, M.J. Lysaght, F.T. Gentile, Transport characterization of membranes for immunoisolation, Biomaterials. 17 (1996) 257–266. https://doi.org/10.1016/0142-9612(96)85563-3.
[35] C. Ronco, P.M. Ghezzi, A. Brendolan, C. Crepaldi, G. La Greca, The haemodialysis system: Basic mechanisms of water and solute transport in extracorporeal renal replacement therapies, Nephrol. Dial. Transplant. 13 (1998) 3–9.
[36] C. Ronco, W.R. Clark, Haemodialysis membranes, Nat. Rev. Nephrol. 14 (2018) 394–410. https://doi.org/10.1038/s41581-018-0002-x.
[37] ANSYS CFX Reference Guide Release 18.2, ANSYS Inc., Canonsburg, PA, USA, 2018., (n.d.).
[38] L. Gurreri, A. Tamburini, A. Cipollina, G. Micale, M. Ciofalo, Flow and mass transfer in spacer-filled channels for reverse electrodialysis: a CFD parametrical study, J.

Memb. Sci. 497 (2016) 300–317. https://doi.org/10.1016/j.memsci.2015.09.006.
[39] R.L. Fournier, Basic Transport Phenomena in Biomedical Engineering, Fourth Edi, CRC Press, Taylor & Francis Group, 2018.
[40] T. Osuga, T. Obata, H. Ikehira, S. Tanada, Y. Sasaki, H. Naito, Dialysate pressure isobars in a hollow-fiber dialyzer determined from magnetic resonance imaging and numerical simulation of dialysate flow, Artif. Organs. 22 (1998) 907–909.